



ON THE OBTAINANCE OF DAMAGE EVOLUTION LAWS FOR COMPOSITE LAMINATES VIA CYCLIC TESTING

Gabriel S. C. Souza^a, Behzad V. Farahani^b, Rui M. Guedes^c, Eduardo Gerhardt^d, Sandro C. Amico^d, Volnei Tita^{a,c}

^aUniversity of São Paulo, São Carlos School of Engineering, Aeronautical Engineering Department Av. João Dagnone, 1100, São Carlos, SP, Brazil, 13563-120 gabrielsales@usp.br, voltita@sc.usp.br

^bGhent University, Department of Electromechanical Systems and Metal Engineering Technologiepark 46, 9052 Zwijnaarde, Gent, Belgium behzad.vasheghanifarahani@ugent.be

^cUniversity of Porto, Faculty of Engineering, Mechanical Engineering Department Rua Dr. Roberto Frias, Porto, Portugal, 4200-465 rmguedes@fe.up.pt, voltita@sc.usp.br

> ^dPPGE3M, Federal University of Rio Grande do Sul Porto Alegre, RS, Brazil, 91501-970 eduardo.gerhardt.eng@gmail.com, amico@ufrgs.br

Keywords: fiber-reinforced composites, continuum damage mechanics, cyclic testing, parameter identification, damage evolution laws.

1. INTRODUCTION

Continuum damage mechanics (CDM) have been used to describe damage development in fiberreinforced plastic (FRP) composite materials since the end of the 1970s and the beginning of the 1980s. CDM considers the emergent effects of intra and interlaminar mechanisms in the material behavior in a lamina. Commonly, deterioration quantification is made via the introduction of damage variables and its kinetics (i.e., evolution or accumulation) predicted by empirical hardening equations obtained from experimental data of quasi-static cyclic testing. From the thermodynamic viewpoint, damage variables (d_{ij}) are state variables having a conjugate thermodynamic force (Y_{ij}) driving their growth. Furthermore, at the meso and macro scales, this translates as a loss of stiffness. Several authors have presented over the years many different CDM-based material models used to describe damage onset and progression for composites. The most comprehensive models are those that consider the different modes present in composites' failure that, in its turn, are dependent on the material stress state. Hence, for each mode, one can expect to exist an evolution law. In particular, during the past 30 years, Ladevèze and contributors [1-3] published several works and developed a constitutive model that describes damage evolution in the composite until final failure. Inspired by these, the present work proposes a different approach to obtain the evolution of damage via cyclic testing for the coupled in-plane shear $(\tau_{12} \neq 0)$ and transverse tension ($\sigma_{22} \ge 0$) case. Instead of the traditional [± 45] and [± 67.5] cross-ply tensile specimens used by Ladevèze and summarized by Herakovich [4], this work proposes utilizing off-axis tensile specimens for this purpose. Also, as already pointed out by Ribeiro [5], the current work supports the finding that for the stress state under study, there exists one damage evolution law for each damage variable that is dependent on the fiber orientation θ , i.e., $d_{22} = f(\theta)$ and $d_{12} = f(\theta)$ in which those are damage variables associated with transverse tension and in-plane shear, respectively.





2. EXPERIMENTAL CAMPAIGN

2.1. Material Set and Specimens' Characteristics

A material set from TORAYCA T700S-12K-50C carbon fiber combined with a UF3369 TCR epoxy resin system is used for all the samples. Manufacture is made by filament-winding (FW) using an MF Tech Kuka robot arm and a flat mandrel, allowing high-quality sample obtaining. Two off-axis orientations (20° and 45°) are selected to be tested under tensile loading. These are chosen due to the existence of low and high coupling between transverse tension and in-plane shear damage mechanisms, as discussed by Sandhu [6]. Specimens' geometry follows recommendations from ASTM D3039 transverse tension sample dimensions, i.e., 175x25x1.85 mm for 20° and 175x25x3.74 mm for 45°. The latter is thicker to avoid fracture at the grips, and, as a rule of thumb, it is recommended a sample thickness of 3.0 to 4.0 mm for all orientations bearing in mind that this is an empirical observation made for laminates with tabs' thickness of 1.5 to 2.0 mm. Herakovich's [4] recommendation that the fibers must not go from one grip to the other for off-axis specimens is respected. Also, the average aspect ratio of the coupons, h/l, equals 14.22, making the global shear stress τ_{xy} negligible, as desired. These are needed for the validity of the considered governing equations and boundary conditions (BCs) of the problem.

2.2. Off-Axis Cyclic Testing

Firstly, to perform cyclic tests, it is necessary to plan these by executing monotonic ones. For this purpose, it was performed three preliminary tests for the 20° and 45° orientations. Also, a maximum of five cycles is permitted to avoid the occurrence of low-cycle fatigue. An INSTRON 5985 universal testing machine and a CANON EOS 350 digital camera are used in all tests to obtain stress and strain histories. The digital camera usage is to analyze the images with the GOM Correlate software of digital image correlation (DIC). All tests are done via machine crosshead displacement control of 0.5 mm/min. Denoting $m = \cos \theta$ and $n = \sin \theta$, and knowing that the experimental setup provides σ_x , ε_x and ε_y , it is possible to obtain all local stress components by:

$$\sigma_1 = m^2 \sigma_x,\tag{1a}$$

$$\sigma_1 = m^2 \sigma_x, \qquad (1a)$$

$$\sigma_2 = n^2 \sigma_x, \qquad (1b)$$

$$\tau_{12} = -mn\sigma_x, \qquad (1c)$$

$$\tau_{12} = -mn\sigma_{x},\tag{1c}$$

and, for the local strain components:

$$\varepsilon_{1} = m^{2} \varepsilon_{x} + n^{2} \varepsilon_{y} + mn \gamma_{xy}, \qquad (2a)$$

$$\varepsilon_{2} = n^{2} \varepsilon_{x} + n^{2} \varepsilon_{y} - mn \gamma_{xy}, \qquad (2b)$$

$$\gamma_{12} = -2mn \varepsilon_{x} + 2mn \varepsilon_{y} + (m^{2} - n^{2}) \gamma_{xy}. \qquad (2c)$$

$$\varepsilon_2 = n^2 \varepsilon_x + n^2 \varepsilon_y - mn \gamma_{xy}, \tag{2b}$$

$$\gamma_{12} = -2mn\varepsilon_r + 2mn\varepsilon_v + (m^2 - n^2)\gamma_{rv}. \tag{2c}$$

To obtain the global shear strain γ_{xy} , it follows that:

$$\gamma_{xy} = \bar{S}_{16}C_2 - \bar{S}_{66}C_0h^2,\tag{3}$$

where h is half the laminate width, C_0 and C_2 are coefficients derived from the solution of the governing equations with constrained BCs. Derivation of these coefficients can be found in [4]. The shear stress in the global coordinate system is given by,

$$\tau_{xy} = \frac{\gamma_{xy} - \bar{S}_{16}\sigma_x}{\bar{S}_{66}},\tag{4}$$



where in Eqs. (3) and (4), \bar{S}_{ij} are the components of the transformed reduced compliance matrix.

3. DAMAGE EVOLUTION LAWS

Stiffness loss is accounted for damage calculation by,

$$d_i = 1 - \frac{E_i}{E_0},\tag{5}$$

in which E_i is the stiffness measured in the *i*-th cycle, E_0 is the elastic modulus and d_i is the damage variable value obtained in the i-th cycle. The thermodynamic forces Y_i associated with each internal damage variable are given as,

$$Y_i = \frac{\sigma_i^2}{[2E_0(1 - d_i)^2]}. (6)$$

From the best fit of experimental data, it is possible to notice that d_i and $\sqrt{Y_i}$ have a linear relationship, i.e., $d_i=a_o\sqrt{Y_i}+a_1$ for each orientation. Denoting by $\sqrt{Y_0}$ and $\sqrt{Y_0'}$ the damage onset thresholds for d_{12} and d_{22} , respectively, these are obtained by imposing $d_{ij} = 0$. Also, the inverse angular coefficients $\sqrt{Y_C}$ and $\sqrt{Y_C'}$ for the in-plane shear and transverse tension are given as $1/a_0$. By doing this, it is possible to retrieve the damage evolution laws by simply,

$$d_{ij} = \frac{\langle \sqrt{Y_{ij}} - \sqrt{Y_0} \rangle}{\sqrt{Y_C}},\tag{7}$$

where the bracket operator simply means that the value inside must be greater than 0. Now, two additional cyclic tests must be executed. These are the pure transverse tension and pure in-plane shear cases and are used to serve as a basis to create four new parameters used to obtain the damage evolution laws for any given angle θ . These are defined as,

$$\alpha_0' = \frac{\sqrt{Y_0'}\big|_{\theta}}{\sqrt{Y_0'}\big|_{\theta=90}},\tag{8a}$$

$$\beta_C' = \frac{\sqrt{Y_C'}|_{\theta}}{\sqrt{Y_C'}|_{\theta=90}},\tag{8b}$$

$$\alpha_0 = \frac{\sqrt{|Y_0|}_{\theta}}{\sqrt{|Y_0|}_{shear}},\tag{8c}$$

$$\beta_C = \frac{\sqrt{|Y_C|_{\theta}}}{\sqrt{|Y_C|_{shear}}},\tag{8d}$$

with Eq. (8a) and (8b) for transverse tension and Eq. (8c) and (8d) for in-plane shear. For each case, a best fit of α_0 and β_C vs. θ is done where, the pure shear result is considered to be $\theta = 10$, since this test can be used to assess shear properties [7]. The parameters dependency with θ are given as:

$$\alpha_0' = -7.5718 * 10^{-4} \theta^2 + 8.5397 * 10^{-2} \theta - 0.5751, \tag{9a}$$

$$\alpha'_0 = -7.5718 * 10^{-4}\theta^2 + 8.5397 * 10^{-2}\theta - 0.5751,$$
(9a)

$$\beta'_C = -2.7417 * 10^{-4}\theta^2 + 4.0035 * 10^{-2}\theta - 0.3814,$$
(9b)

$$\alpha_0 = -2.0162 * 10^{-4}\theta^2 + 3.0809 * 10^{-3}\theta + 1.3192,$$
(9c)

$$\alpha_0 = -2.0162 * 10^{-4}\theta^2 + 3.0809 * 10^{-3}\theta + 1.3192, \tag{9c}$$





$$\beta_C = -3.4225 * 10^{-4}\theta^2 + 2.0842 * 10^{-2}\theta + 0.8894. \tag{9d}$$

Also, Tab. 1 shows the results obtained along with Fig. 1.

Table 1 – Parameters values for each case.

Orientation	Transverse tension				In-plane shear			
	$\sqrt{Y_0'}$	$\sqrt{Y_C'}$	$lpha_0'$	$oldsymbol{eta}_{oldsymbol{c}}'$	$\sqrt{Y_0}$	$\sqrt{Y_c}$	$lpha_0$	$\boldsymbol{\beta}_{c}$
Shear (10°)	n/a	n/a	0	0	0.14412	1.03681	1	1
20°	0.05987	0.38377	1.15488	0.29612	0.26351	1.31763	1.82845	1.27084
45°	0.08244	1.12938	1.59037	0.87143	0.11746	1.12939	0.81500	1.08929
90°	0.05184	1.29602	1	1	n/a	n/a	0	0

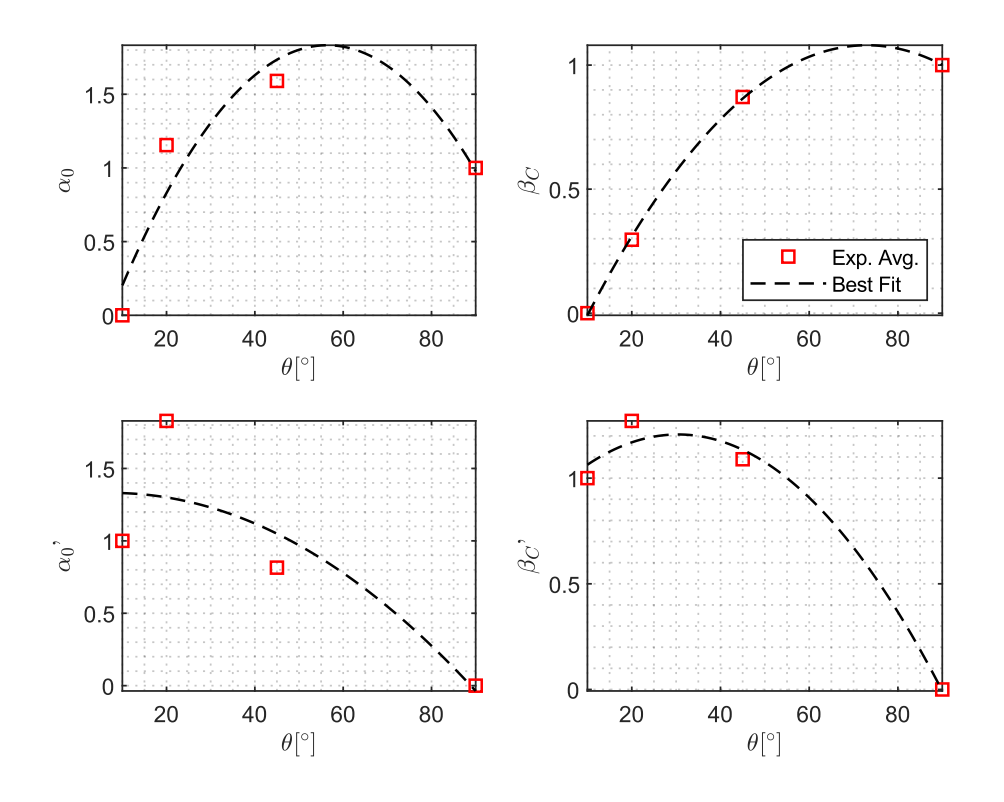


Figure 1 – Experimental data of α_0 , α'_0 , β_C , β'_C vs. θ and best fit.

Therefore, for any given θ it is possible to obtain the α and β parameters from Eq. (9). Now, using Eq. (8), the damage onset thresholds and the inverse angular coefficients are obtained and using Eq. (7) it is possible to predict the damage variable value of interest, and, consequently, to obtain its damage evolution law as depicted in Fig. 2.

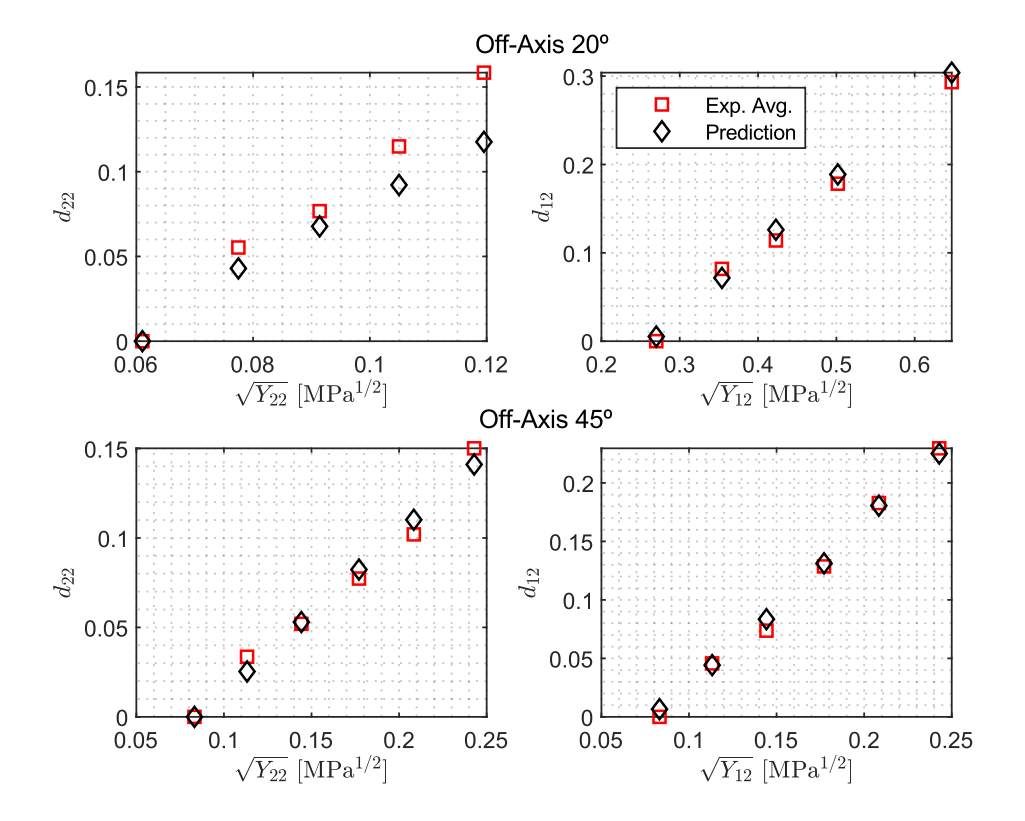


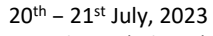
Figure 2 – Decoupled damage evolution for tensile off-axis laminates: experimental results and prediction.

4. FINAL REMARKS

The present work objective was to derive the damage evolution relations for any fiber angle θ from a few cyclic tests considering the coupling between transverse tension and in-plane shear mechanisms. To accomplish this, four cyclic tests are necessary, two of these on off-axis laminates that, in this study, are chosen to be with 20° and 45° orientation. The other two remaining tests are for the pure transverse tension and in-plane shear cases used for the definition of four new parameters used to predict the damage evolution law for an arbitrary orientation. After applying the step-by-step approach to retrieve the damage variables values, is observed a good behavioral and quantitative agreement for all case studies, the worst one being for d_{22} in the 20° case. It is also noticeable that the damage evolution is not the same for different angles, which is supported by Ladevèze et al. [1-3] but dealt in a different manner, and in agreement with observations of Ribeiro [5]. Recommendations for the specimens' geometry are made based on the necessity to perform more tests on thicker 20° laminates due to failure at the tab area, a feature observed on thinner 45° laminates too. The main advantage of the present approach is the simplicity of tests and the ease to manufacture laminates without adding many experiments in comparison with other methodologies. Furthermore, the present approach needs to be tested for different damage mechanisms, for example, in the $\sigma_{22} < 0$ portion of the $\sigma_{22} - \tau_{12}$ envelope.

ACKNOWLEDGEMENTS

The authors acknowledge the financial support of the Coordination for the Improvement of Higher Education Personnel (CAPES numbers 88887.608253/2021-00, 88887.817120/2023-00 and 88887.729128/2022-00). Volnei Tita is thankful for the support of CAPES (CAPES-FCT: AUXPE 88881.467834/2019-01) — Financial Code 001. The FAPESP-FAPERGS project (process number: 2019/15179-2 and 19/2551) is also acknowledged.





REFERENCES

- [1] P. Ladevèze, E. LeDantec. Damage modelling of the elementary ply for laminated composites. Composites science and technology, v. 43, n. 3, p. 257-267. (1992).
- [2] O. Allix, P. Ladevèze. Interlaminar interface modelling for the prediction of delamination. Composite Structures, Elsevier, v. 22, n. 4, p. 235-242. (1992).
- [3] O. Allix, P. Ladevèze, A. Corigliano. Damage analysis of interlaminar fracture specimens. Composite Structures, Elsevier, v.31, n. 1, p. 61-74. (1995).
- [4] C. T. Herakovich. *Mechanics of fibrous composites*. John Wiley & Sons. (1998).
- [5] M. L. Ribeiro. Damage and progressive failure analysis for aeronautic composite structures with curvature. PhD Thesis. University of São Paulo. (2013).
- [6] R. Sandhu. Nonlinear behavior of unidirectional and angle ply laminates. *Journal of Aircraft*, v. 13, n. 2, p. 104-111. (1976).
- [7] M. Merzkirch, T. Foecke. 10° off-axis testing of CFRP using DIC: A study on strength, strain and modulus. Composites Part B: Engineering, v. 196, p. 108062. (2020).

RESPONSIBILITY NOTICE

The author(s) is (are) the only responsible for the printed material included in this manuscript.



REDUCTION OF PLATE FLEXIBILITY BY THE PROGRESSIVE APPLICATION OF REINFORCEMENTS WITH OPTIMIZED PATHS

Eduardo da Rosa Vieira^a, Daniel Milbrath de Leon^b, Rogério José Marczak^b

^aFederal Institute of Rio Grande do Sul – IFRS – Campus Rio Grande 475 Eng. Alfredo Huck St, Rio Grande, 96201-460, Brazil vieira.r.eduardo@gmail.com

^bFederal University of Rio Grande do Sul – UFRGS – PROMEC 425 Sarmento Leite St, Porto Alegre, 90040-001, Brazil daniel.leon@ufrgs.br; rato@mecanica.ufrgs.br

Keywords: Optimization, Reinforced Plates, Stiffeners, VAT, Linear Programming

1. INTRODUCTION

The elaboration of equipment projects using plates and shells as structural elements is very common in the mechanical industry, especially in shipbuilding and aircraft. However, as these elements are generally thin, their ability to withstand high loads without collapsing is relatively low [1,2]. Therefore, one of the solutions to improve the mechanical properties is to increase its thickness. This design suitability ends up causing a significant increase in structural weight, reducing the ratio between weight and resistance and designing low energy efficiency systems. Another solution is the insertion of reinforcements in the plates, which improve the structure's performance, mainly increasing the stiffness and critical buckling load, in addition to reducing tension and deformation [2,3].

Generally, most of the structural elements are constructed of steel or other metals, as well as the reinforcements, which are normally attached to the surface of the plates by welding. These reinforcements are also called stiffeners [2]. The more traditional stiffeners are produced in geometries that allow their positioning orthogonal to the plate, with rectilinear lengths and equidistant positioning from each other [4]. These reinforcements provide considerable improvement in mechanical properties, with relatively low insertion of material, developing structures with lower cost and better ratio between weight and strength [5].

The replacement of metallic materials by composites is a reality in the mechanical industry, and some aircraft models already have more than 50% of composites in their structure. This is because these materials have excellent reliability and a high weight-to-strength ratio. In this context, fiber-reinforced polymer matrix composites are the most prominent [3,6]. In addition, the development of manufacturing techniques that allowed the construction of curvilinear fibers made possible the applications of these composites. The ability to build plates with independent reinforcements in each layer, the Variable Angle Tow (VAT), made it possible to explore the anisotropy of composites in order to design structures that are more adapted to each project [7,8]. Furthermore, in order to obtain the best positioning of the reinforcements, it is essential to apply an optimization method. In this way, excellent results can be achieved without an increase in the volume of reinforcements [9].

Plates with stiffeners made of fibrous composite materials - with a polyester matrix and fiberglass reinforcement - were designed and experimentally validated, demonstrating the possibility of using these materials as stiffeners. In several cases tested, an increase of between 38% and 110% was observed in its resistance to flexion load in relation to plates without stiffeners [5]. Alhajahmad and Mittelstedt (2020) successfully employed path optimization of plate stiffeners, which resulted in curvilinear reinforcements. However, these reinforcements were external to the matrix and their trajectories were not mutually independent, resulting in parallel and equidistant paths [10]. In turn, Esposito *et al.* (2019) studied plates built with an epoxy resin matrix and carbon fiber reinforcements, which were internal to the plate. It should be noted that, in these experiments, the authors used an unrestricted number of fibers, which occupied almost the entire area of the structure. In one of the case studies of the work, a cantilever



plate with optimized reinforcement trajectories, under a point load, reduced flexibility by 56.03% in relation to a quasi-isotropic plate, which had the same geometry and the same boundary conditions [11].

As new manufacturing technologies make it possible to manufacture reinforcements with considerable variation in cross-sectional area, it is possible to build stiffeners that remain internal to the structure. Thus, using a reduced number of filaments, which when they have optimized paths, enable a significant reduction in flexibility [11,12]. Therefore, this work aims to reduce the flexibility of a plate containing a limited number of reinforcements. These stiffeners are progressively deposited and optimized, until the increase in the number of reinforcements does not present significant results for minimizing the total flexibility of the structure.

2. METHODOLOGY

The aim of this work is to reduce the flexibility of an epoxy resin plate reinforced by carbon fibers. The plate used has the same geometry and boundary conditions used by Esposito *et al.* (2019), which had a height of 200 mm, length of 500 mm and thickness of 2.24 mm. In addition, it was fixed on one of the vertical edges and on the other edge a vertical load of 1 kN was applied. The structure can be seen in Figure 1(a). Before applying reinforcements, the plate will have its compliance calculated. After that, reinforcement with a square cross section will be applied. The edge of the cross-section has the same dimension as the plate thickness. This fiber has a horizontal initial direction, is located between the upper and lower ends of the plate and its center coincides with the median plane. This structure can be seen in Figure 1(b).

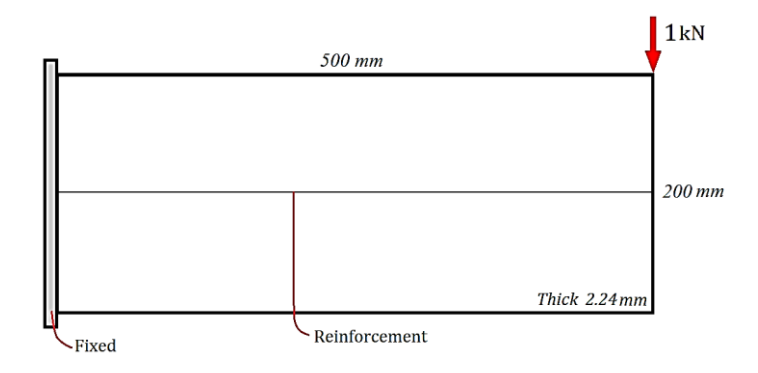


Figure 1 – Plate with boundary conditions and a reinforcement at the starting position

The reinforcement paths are represented by B-Splines and have their trajectory optimized by Linear Programming. The flexibility of the structure will be measured by its total strain energy, which is calculated by the Finite Element Method.

The applied process starts with the deposition of this rectilinear reinforcement on the plate, followed by the optimization of its trajectory. After this reinforcement has been optimized, it is kept in the position obtained and a new straight reinforcement is applied in the same initial horizontal position and is also optimized. This process is repeated until the insertion and optimization of new fibers does not cause significant improvement in reducing the flexibility of the structure.

3. RESULTS AND DISCUSSION

First, before the implementation of reinforcements, the deformation energy of the plate without any reinforcement was calculated. Based on the assessment of the non-reinforced plate, the stiffeners were implemented in the standardized initial position and at each insertion and subsequent optimization of the fiber, the strain energy was recorded. Then, in order to compare the effects caused by the application of more filaments, the percentages of reduction of the strain energy in relation to the structure composed only of epoxy resin were calculated. These results are shown in Figure 2.

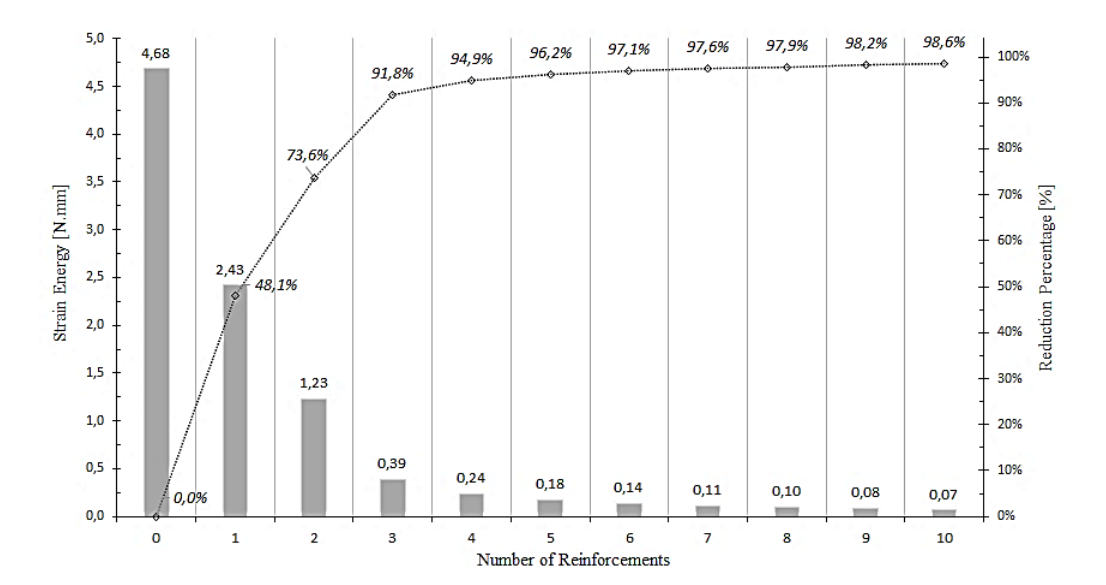


Figure 2 – Strain energy and percentage reduction for each number of reinforcements applied

As can be seen in the graph, the board without reinforcements has compliance equal to 4.68 Nmm. When a single reinforcement is placed and optimized, the strain energy has a value equal to 2.43 Nmm, which represents a percentage reduction of 48.1% in the flexibility of the structure. After that, the insertion of the second stiffener has a significant effect, but less than the previous reinforcement. The third reinforcement also exhibits a relatively large minimization of strain energy. In turn, the fourth reinforcement still develops a considerable reduction in the flexibility of the plate, however, its percentage reduction is only 3.1%. This minimization is low compared to the second and third stiffeners, which reduced by 25.5 and 18.2% respectively.

From the fifth reinforcement, there is no justification for implementing a greater number of reinforcements. This occurs because, in the observed cases, there is no percentage reduction in strain energy greater than 1.3%, and the increase in the number of reinforcements no longer produces significant effects on the flexibility of the structure. Furthermore, the fibers begin to occupy equal or very close positions on the plate. Added to this, it is possible to notice that a very high number of crossings between the fibers begins to occur, which may cause greater difficulty in the fabrication of the structures. Figure 3 presents the results of the plate with four and ten stiffeners.

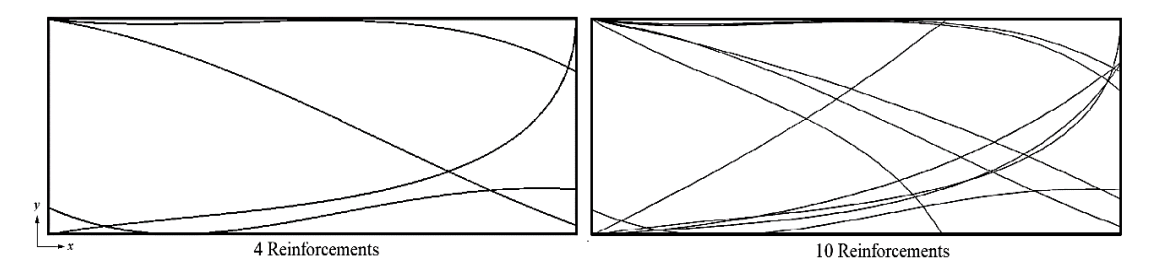


Figure 3 – Path of optimized reinforcements on plates with four and ten stiffeners

According to the results obtained, it is possible to understand that for the structure studied under the imposed boundary conditions, there is no justification for using a number greater than four reinforcements. It is important to highlight that this number of reinforcements is specific to the case study investigated in this work. Therefore, in other structures, materials or boundary conditions, it is necessary to verify the ideal number of stiffeners. Since, due to the anisotropic characteristics of these materials, it is possible that a different number of reinforcements is more appropriate.



4. CONCLUSIONS

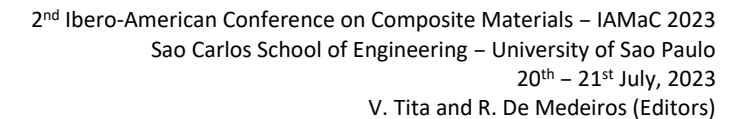
- It is possible to greatly reduce the flexibility of plates using a relatively low number of reinforcements with optimized paths.
- The capacity to reduce the strain energy is inversely proportional to the number of reinforcements inserted in the plate, that is, the greater the number of reinforcements applied, the lower the capacity to reduce the strain energy.
- In the studied structure, the application of more than four reinforcements is not indicated, a number equal to or greater than five reinforcements do not cause a significant effect on the plate.
- High amounts of stiffeners, in addition to not producing a significant reduction in flexibility, also cause many crossings between the fibers, which can make it difficult to manufacture structures.

ACKNOWLEDGEMENTS

This study was financed in part by the Coordenação de Aperfeiçoamento de Pessoal de Nível Superior – Brasil (CAPES) – Finance Code 001. This study was carried out with the support of the Conselho Nacional de Desenvolvimento Científico e Tecnológico (CNPq), under the grant number 140478/2020-5, and Fundação de Amparo à Pesquisa do Estado do Rio Grande do Sul (FAPERGS), under the grant number 19/2551-0001255-1.

REFERENCES

- [1] M. M. Alinia. A study into optimization of stiffeners in plates subjected to shear loading. *Thin-Walled Structures*, v.43, December. (2005).
- [2] R.S. Shirazi, M.M. Alinia. On the design of stiffeners in steel plate shear walls. *Journal of Constructional Steel Research*, v.65, June. (2009).
- [3] S. Kesarwani. Polymer Composites in Aviation Sector. *International Journal of Engineering Research*, v.6. (2017).
- [4] D.J. Mead. Plates with regular stiffening in acoustic media: Vibration and radiation. *The Journal of the Acoustical Society of America*, v.88. (1990).
- [5] T. I. Thinh, T. H. Quoc. Finite element modeling and experimental study on bending and vibration of laminated stiffened glass fiber/polyester composite plates. *Computational Materials Science*, v.49. (2010).
- [6] J. Konieczny, K. Labisz. Materials Used in The Combat Aviation Construction. *Transport Problems*, v.16. (2021).
- [7] S.B. Aragh. et al. Manufacturable Insight into Modelling and Design Considerations in Fibre-Steered Composite Laminates: State of the Art and Perspective. *Computer Methods in Applied Mechanics and Engineering*, v. 379. (2021).
- [8] Z. Wu, G. Raju, P.M. Weaver. Optimization of Postbuckling Behaviour of Variable Thickness Composite Panels with Variable Angle Tows: Towards "Buckle-Free" Design Concept. *International Journal of Solids and Structures*, v.132, September. (2018).
- [9] S. Nikbakt, S. Kamarian, M. Shakeri. A Review on Optimization of Composite Structures Part I: Laminated Composites. *Composite Structures*, v.195, March. (2018).
- [10] A. Alhajahmad, C. Mittelstedt. Design Tailoring of Curvilinearly Grid-Stiffened Variable-Stiffness Composite Cylindrically Curved Panels for Maximum Buckling Capacity. *Thin-Walled Structures*, v.157. (2020).
- [11] L. Esposito, et al. Topology Optimization-Guided Stiffening of Composites Realized through Automated Fiber Placement. *Composites Part B*, v.164, September. (2019).
- [12] M.A. Albazzan, et al. Efficient Design Optimization of Nonconventional Laminated Composites using Lamination Parameters: A State of the Art. *Composite Structures*, v.209. (2019).





RESPONSIBILITY NOTICE

The author(s) is (are) the only responsible for the printed material included in this manuscript.



STUDY OF FILAMENT WOUND CYLINDERS WITH VAT IN ELASTIC CONDITIONS

Maísa Milanez Ávila Dias Maciel ^a, Bruno Cristhoff ^a, Sandro Amico ^b, Eduardo Gehardt ^b, Nuno Viriato Ramos ^c, Paulo Tavares ^c, Rui Miranda Guedes ^c, Volnei Tita ^a

^aUniversitty of São Paulo Sao Carlos School of Engineering, Brasil, 13563-120 maisa.madm@usp.br, brunogch@gmail.com, voltita@usp.br

^b Federal University of Rio Grande do Sul Porto Alegre, Brasil, 90040-060 eduardo.gerhardt.eng@gmail.com, 00146425@ufrgs.br

° Porto University, Faculty of Engineering Porto, Portugal nviriato@inegi.up.pt, ptavares@inegi.up.pt, rmguedes@fe.up.pt

Keywords: variable angle tow, variable stiffness, VIC 3D, elastic testing, radial compression

1. INTRODUCTION

Carbon fiber reinforced polymers (CFRP) have been widely used not only in secondary structures, but also as primary structures in aircraft [1,2]. On the other hand, the maximum potential of composites is still not utilized, since the only factor considered for composite designs is the high specific strength and stiffness. However, the opportunity to design the structural components considering factors such as anisotropy and the dependence of the fiber architecture on fracture resistance is lost [3].

Traditionally, CFRP are manufactured with an almost isotropic behavior [4]. However, this type of conventional architecture does not fully exploit its anisotropy. Thus, placing the fibers in a continuous and smooth curved path [5–8] can optimize the use of CFRP. These fiber laminates with a curved trajectory are denominated as variable angle tow (VAT), which shows fibers that vary their orientation according to their coordinates in the plane of the lamina [6,9,10].

VAT have shown promising uses in the aeronautical and aerospace industry, due to the increase in resistance to buckling and behavior against vibrations due to their ability to redistribute loads from critical regions to the interior of the laminate [9,11–15]. However, due to the heterogeneous and anisotropic characteristics, different types of occur, leading to very complex mechanical behavior [9]. As the only way to use these materials in primary structures in a safe way is by knowing the initiation and propagation of damage, it becomes essential to study the mechanisms of initiation, propagation, and prediction of damage. VAT present two types of imperfections arising from processing methods, which are resin pockets (gaps) and overlapping reinforcements (overlaps). These imperfections can be hotspots for damage nucleation from mechanical deformations. Within the context of the aeronautical and aerospace industry, this proposal therefore aims to contribute to the development of advanced composite structures without interfering with aircraft safety. The use of VAT laminates can reduce the weight of structures, allowing energy savings for aircraft.

2. METODOLOGY

In this work cylindrical shells of variable stiffness were manufactured by FW using the KUKA KR 140 L100 robot integrated with the MF-Tech control system. The towpreg used is by TCR



composites, in which the filaments are by Toray T700-12K-50C with UF3369 resin system. Unidirectional resistance values were previously obtained and are found in references [21,22]. The cylinders are 130 mm in diameter and the angle variation is $52^{\circ}/62^{\circ}(\alpha 0)/52^{\circ}$ ($\alpha 1$, with two of the three cylinders having a length of 150mm and one of them having a length of 200mm. In addition, they have different winding tension, with 75% and 50%, these variations being in order to reach a more suitable processing condition.

2.1. Radial Compression

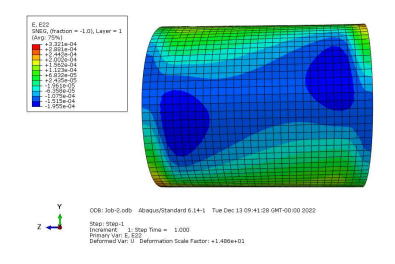
The static tests performed is radial compression within the elastic regime with a load ratio of 20 N/min up to a maximum load of 110 N. The test was carried out in two stages, firstly the loading ramp, which presented a pre – load of 0.5 N and ending with 110 N. After the ramp there was a landing where the load is maintained at 110 N for 30 s. The test lasted 6 min in total. The testing was accompanied by digital image correlation 3D due to the materials curvature [23]. The software, Vic3D, performed the acquisition at 45 Hz, but the images were selected later. Spatial resolution was 06 μ m/pixel with objective lenses of 60 mm focal length.

2.2. Simulation parameters

The material has 4 layers and approximately 2 mm, and was assumed to have an orientation of 57° (the average between the two maximum angle variations). 3 integration points were used for each layer. At the bottom of the cylinder the following degrees of freedom were restricted u2 = ur1 = ur3 = 0. A displacement of 0.07 mm and 0.5mm was applied to the nodes at the top of the cylinder. The value of 0.07 mm is related to 10% of the maximum displacement of the 90° compression test performed on unidirectional samples of the same material. After that, the displacement was increased until a limiting condition given by the Hashin criterion was found. To determine when a material would be 'degraded', the damage initiation model for FRP based on Hashin's theory [24,25] was used, which considers 4 failure modes, fiber traction, fiber compression, traction, and matrix compression, and is already implemented in the ABAQUS distribution. Thus, by using a damage variable, a value of 1.0 or higher indicates that the initiation criterion has been met, so that the propensity of the material to suffer damage can be evaluated without modeling the damage evolution process, considering thus the first ply failure instead of the last ply failure.

3. RESULTS AND DISUSSIONS

It was obtained that the maximum force for 1 mm of displacement was 179 N in the direction of 52°, which would be on the edge of the cylinder, and the maximum value of the Hashin coefficient was in the direction of traction of the matrix and its value was of 0.017. In the tests, the value of 110 N will be used for the maximum load, and the load application rate will be approximately 22 N/min. Figure 1 show the strain map in the 2 (y) direction and the Hashin coefficients map in matrix compression mode, which was the most severe condition found in the simulation. These are the first maps that will be compared with the values obtained by the DIC.



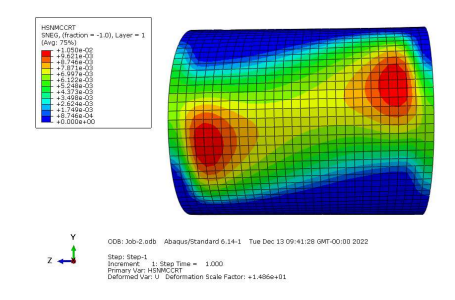






Figure 1. Strain map in direction 2, in side view (y-z plane) and the Hashin coefficients map in compression mode for matrix in side view (y-z plane)

The observed displacements obtained experimentally were close to the one obtained by the simulations for the predicted load in the test. With the 200:75 cylinder having a final displacement of 1.0mm and the 150:50 cylinder having a final displacement of 1.3mm.

Figure 2 shows the final states of deformation in the Y direction, for cylinders 150:50, 150:75 and 200:75, obtained by DIC 3D

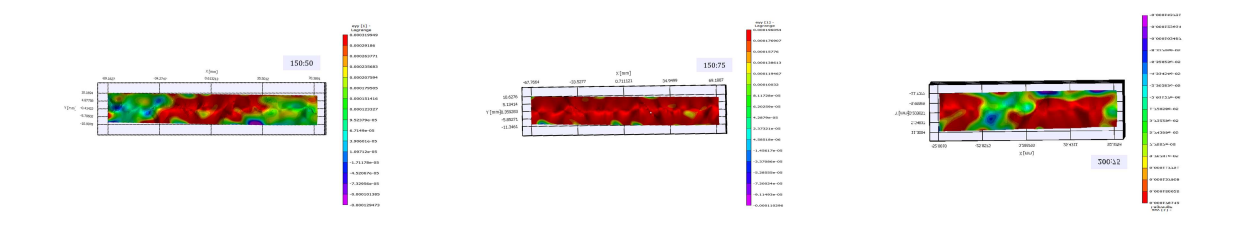


Figure 2 Deformation maps in the Y direction for cylinders 150:50, 150:75 and 200:75

Firstly, it is important to note that only for the 200:75 cylinder, the map only represents half of the cylinder because the length of 200 mm did not allow framing by the lens. At first, there was no correlation between the images, but the observation tracks were made at different points of the cylinder, which may have led to different effects being present in the deformation map, since, according to the literature, the winding pattern of the cylinder can considerably increase the stresses along the length [26]. Furthermore, the literature suggests that winding patterns change stress distributions to non-linear distributions and alter fracture processes of regions [26–28]. It is observed that for cylinder 150:75 the analysis was performed almost to the center of the pattern and for cylinders 150:50 and 200:75 the analysis was displaced from the center of the winding patterns.

4. CONCLUSIONS

Cylinders manufactured with a winding of 52° at the ends and 62° at the center were analyzed in the elastic region by finite elements and with a radial compression test. Simulation analyzes showed a maximum flexion of 1 mm for a load of 110 N which was very close to that obtained for all cylinders 1.0 mm, 1.3 mm and 1.3 mm for cylinders 150:50, 150:75 and 200:75 respectively. The simulation also resulted in a deformation map in the y direction, showing mostly compressive deformations. The experimental radial compression tests, however, show that the cylinders present mainly tensile deformation in the y direction, but that the winding pattern together considerably influences the pattern of the deformation map, which may have affected the results for comparison.

ACKNOWLEDGEMENTS

We would like to acknowledge the founding of FAPESP/FAPERGS and CAPES/FCT number 88887.660187/2021-00. The first author would also like to acknowledge the CAPES PROEX number 88887.817112/2022-00.

REFERENCES

Okabe T. Recent studies on numerical modelling of damage progression in fibre-reinforced plastic composites. Mechanical Engineering Reviews 2015;2:14-00226-14-00226. https://doi.org/10.1299/mer.14-00226.



- [2] Djabali A, Toubal L, Zitoune R, Rechak S. An experimental investigation of the mechanical behavior and damage of thick laminated carbon/epoxy composite. *Compos Struct* 2018;184:178–90.
- [3] Fanteria D, Lazzeri L, Panettieri E, Mariani U, Rigamonti M. Experimental characterization of the interlaminar fracture toughness of a woven and a unidirectional carbon/epoxy composite ScienceDirect. *Compos Sci Technol* 2017;142:20–9.
- [4] Uhlig K, Tosch M, Bittrich L, Leipprand A, Dey S, Spickenheuer A, et al. Meso-scaled finite element analysis of fiber reinforced plastics made by Tailored Fiber Placement. *Compos Struct* 2016;143:53–62.
- [5] Tornabene F, Fantuzzi N, Bacciocchi M. Foam core composite sandwich plates and shells with variable stiffness: Effect of the curvilinear fiber path on the modal response. *Journal of Sandwich Structures and Materials* 2019;21:320–65
- [6] Gürdal Z, Tatting BF, Wu CK. Variable stiffness composite panels: Effects of stiffness variation on the in-plane and buckling response. *Compos Part A Appl Sci Manuf* 2008;39:911–22.
- [7] Gürdal Z, Olmedo R. In-plane response of laminates with spatially varying fiber orientations: Variable stiffness concept. AIAA/ ASME/ASCE/AHS/ASC 33rd Structures, Structural Dynamics, and Materials Conference, vol. 31, Dallas: 1993, p. 751–8.
- [8] Blom AW, Abdalla MM, Gürdal Z. Optimization of course locations in fiber-placed panels for general fiber angle distributions. *Compos Sci Technol* 2010;70:564–70.
- [9] Soriano A, Díaz J. Failure analysis of variable stiffness composite plates using continuum damage mechanics models. *Compos Struct* 2018;184:1071–80.
- [10] Montemurro M, Catapano A. A general B-Spline surfaces theoretical framework for optimisation of variable angle-tow laminates. *Compos Struct* 2019;209:561–78.
- [11] Sousa CS, Camanho PP, Suleman A. Analysis of multistable variable stiffness composite plates. *Compos Struct* 2013;98:34–46.
- [12] Almeida JHS, Bittrich L, Jansen E, Tita V, Spickenheuer A. Buckling optimization of composite cylinders for axial compression: A design methodology considering a variable-axial fiber layout. *Compos Struct* 2019;222:110928.
- [13] Uhlig K, Bittrich L, Spickenheuer A, Almeida JHS. Waviness and fiber volume content analysis in continuous carbon fiber reinforced plastics made by tailored fiber placement. *Compos Struct* 2019;222:110910.
- [14] Yazdani S, Ribeiro P, Rodrigues JD. A p-version layerwise model for large deflection of composite plates with curvilinear fibres. *Compos Struct* 2014;108:181–90.
- [15] Yazdani S, Ribeiro P. A layerwise p-version finite element formulation for free vibration analysis of thick composite laminates with curvilinear fibres. *Compos Struct* 2015;120:531–42.
- [16] Almeida Júnior JHS, Staudigel C, Caetano GLP, Amico SC. Engineering properties of carbon/epoxy filament wound unidirectional composites. 16th European Conference on Composite Materials, ECCM 2014, Seville: 2014, p. 22–6.
- [17] Almeida Júnior JH, Maciel MMÁ dias, Tita V. Effect of Imperfect Fiber/Matrix Interphase: a Micromechanical Model for Predicting Failure in Composite Materials. ABCM International Congress of Mechanical Engineering, Uberlândia: 2019. https://doi.org/10.26678/abcm.cobem2019.cob2019-0623.
- [18] Gu Y, Zhang D, Zhang Z, Sun J, Yue S, Li G, et al. Torsion damage mechanisms analysis of two-dimensional braided composite tubes with digital image correction and X-ray micro-computed tomography. *Compos Struct* 2021;256:113020..
- [19] Hashin Z. Failure Criteria for Unidirectional FibreComposites. J Appl Mech 1980;47:329–34.
- [20] Hashin Z, Rotem A. A Fatigue Failure Criterion for Fiber Reinforced Materials. *J Compos Mater* 1973;7:448–64.
- [21] Morozov E v. The effect of filament-winding mosaic patterns on the strength of thin-walled composite shells. *Compos Struct* 2006;76:123–9.
- [22] Mian HH, Rahman H. Influence of mosaic patterns on the structural integrity of filament wound composite pressure vessels. *International Journal of Structural Integrity* 2011;2:345–56.
- [23] Stabla P, Lubecki M, Smolnicki M. The effect of mosaic pattern and winding angle on radially compressed filament-wound CFRP composite tubes. *Compos Struct* 2022;292.

RESPONSIBILITY NOTICE

The author(s) is (are) the only responsible for the printed material included in this manuscript.



A TECHNIQUE FOR STRUCTURAL FINITE ELEMENT MODELING OF FIBER-REINFORCED RUBBER COMPOSITE USED IN FLEXIBLE **COUPLINGS**

Bruno Cavalli Vieceli^a, Katulo Rossi De Martini Moraes ^a, Daniel Pacheco e Silva ^a, João Moreira Lopes ^a, Lourenço de Siqueira Daudt ^a, Filipe Paixão Geiger ^a, Rogério José Marczak ^a

> ^aFederal University of Rio Grande do Sul – UFRGS Av. Paulo Gama, 110, Porto Alegre 90040-060, Brazil bruno.vieceli@ufrgs.br 00288467@ufrgs.br 00318380@ufrgs.br 00323852@ufrgs.br lourenco.daudt@ufrgs.br filipe.geiger@ufrgs.br rato@mecanica.ufrgs.br

Keywords: fiber-reinforced elastomer, tire coupling, anisotropic hyperelasticity

1. INTRODUCTION

Fiber-reinforced elastomer composites see a wide range of applications in today's industry. One of the most common for these types of composites are seen in tires, as they contain several reinforcements made of steel wires and fiber plies, along with the rubber. Other applications may be seen on aerospace sectors [1] but also on the analysis of biological soft tissues [2-3], as they tend to be well represented by a soft matrix which is strengthened by internal fibers. The focus, however, will be on the analysis of a tire or tyre coupling, which consists of a fiber-reinforced rubber part which is vulcanized together with a steel flange. The flange is typically joined with a steel hub via a bolted connection, as per Fig. 1. The main function of such component is to transmit power and torque between two shafts that have some radial and/or angular misalignments between them.

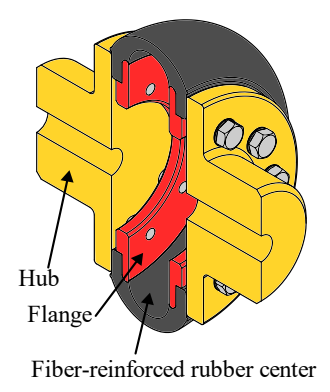


Figure 1 – View cut of isometric drawing of tire coupling.

In order to develop a structural analysis for this component, one must consider the hyperelastic behavior of the rubber matrix, as well as the linear elastic, anisotropic behavior of the fiber reinforcement. Some works have been done on the subject, mainly to develop a hyperelastic model



which accounts for internal fiber direction. [4] managed to utilize overlay "rebar" finite elements in the context of large strains to represent the reinforcements in a composite material. [5] managed to implement a transversely isotropic hyperelastic constitutive model in small to moderate strains in a finite element simulation, requiring traction, shear and two compression tests for calibration. [6-7] also developed anisotropic hyperelastic models, but with applications for textile fabrics in forming simulation and shape memory composites, respectively. [8] proposed another model, but with applications to coord-rubber composites (mainly tires) with good agreement to experimental data. [9] performed a numerical simulation in a fiber-reinforced rubber V-belt through an adaptation of the Mooney-Rivlin model, to include the transverse effects.

All the works presented have been used for simple geometry cases or are not yet available in a commercially viable solution, requiring complex and time-consuming implementations. In this regard, this work aims to perform a structural finite element analysis in a tire coupling through simple assumptions, considering different techniques for modelling its behavior, which impacts the CAD drawings, hyperelastic model choice and methodology for calibration of hyperelastic model. The results are subsequently compared to experimental tests, in order to assess the validity of the numerical analysis.

2. METHODOLOGY

2.1. Finite elasticity and hyperelastic formulation

When dealing with structures characterized by large displacements, rotations, and deformations, as it is common for hyperelastic problems, formulations for finite elasticity must be considered. In the more general sense, consider an undeformed body Ω_0 , as per Fig. 2(a), which lies in a stress-free configuration and in the absence of body forces. The body is mapped by a material point vector $\mathbf{X} \in \Omega_0$. Under the action of a traction field \mathbf{t}_0 and displacement field \mathbf{u}_0 , the body encounters a deformation map $\chi: \Omega_0 \to \Omega$ that establishes a deformed configuration Ω with displacements $\mathbf{u}(\mathbf{X})$, seen in Fig. 2(b), and is now defined by the material point vector $\mathbf{x} = \chi(\mathbf{X})$. This leads to the definition of a deformation gradient field $\mathbf{F} = \partial \mathbf{x}/\partial \mathbf{X}$ and the right Cauchy-Green strain tensor $\mathbf{C} = \mathbf{F}^{\mathrm{T}}\mathbf{F}$.

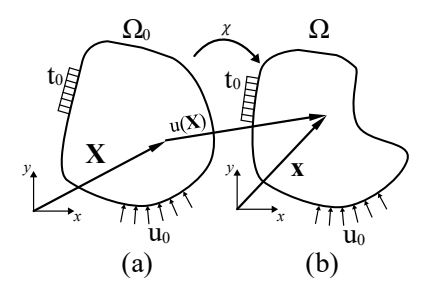


Figure 2 – Schematic drawing of a body in (a) undeformed configuration; (b) deformed configuration.

The strain energy Ψ can be defined as a function of \mathbf{C} , as in $\Psi = \Psi(\mathbf{C})$. In hyperelasticity, it is common to also write this function in terms of the invariants I_1 , I_2 and I_3 , for an isotropic material. However, since anisotropy is present, one must also add at least one pseudo-invariant, I_4 , which accounts for fiber direction.

Many models aim to define the strain function Ψ. The Holzapfel-Gasser-Ogden (HGO) model [10] is a known anisotropic model which also includes the I_6 pseudo-invariant. In Abaqus® implementation, however, I_6 is discarded and Ψ takes the form of Eq. (1), with \bar{E}_{α} defined in Eq. (2).

$$\Psi = C_{10}(\bar{I}_1 - 3) + \frac{1}{D} \left(\frac{J^2 - 1}{2} - \ln J \right) + \frac{k_1}{2k_2} \sum_{\alpha = 1}^{N} \left(\exp\left\{ k_2 \left[\frac{1}{2} (|\bar{E}_{\alpha}| + \bar{E}_{\alpha}) \right]^2 \right\} - 1 \right)$$
 (1)

$$\bar{E}_{\alpha} = \kappa(\bar{I}_1 - 3) + (1 - 3\kappa)(\bar{I}_{4(\alpha\alpha)} - 1)$$
(2)

V. Tita and R. De Medeiros (Editors)

 C_{10} , D, k_1 , k_2 and κ are material parameters to be calibrated, N is the number of families of fibers, \bar{I}_1 is the first invariant of $\bar{\mathbf{C}} = J^{-\frac{2}{3}}\mathbf{C}$, $J = \det \mathbf{F}$ is the Jacobian and $\bar{I}_{4(\alpha\alpha)}$ are the fourth pseudo-invariant of $\bar{\mathbf{C}}$ and \mathbf{a}_{α} , $\bar{I}_{4(\alpha\alpha)} = \mathbf{a}_{\alpha} \cdot \bar{\mathbf{C}} \cdot \mathbf{a}_{\alpha}$, where \mathbf{a}_{α} are a set of unit vectors in the direction of fibers in the reference configuration.

2.2. Hyperelastic model calibration

The tire coupling has two sets of reinforcements embedded in the rubber in the form of woven fabrics, each set containing a fabric at the 45° and 135° angles relative to the toroidal surface of the coupling (that is, four fabrics in total).

To fit the data, MCalibration® software is used. The HGO model requires at least two curves to calibrate the entire set of material parameters. This is typically done with a sample with the fibers in the 1-direction and the other at the 2-direction. This is not possible in this case since there are multiple reinforcements in different directions. To overcome such a problem and fit the elastomer-reinforcement material to the Holzapfel-Gasser-Ogden form, a set of tensile test coupon specimens are created, one of which contains the fabric in the $[0/90]_2$ configuration, and the other at $[45/135]_2$ configuration. The stress-strain curves for the specimens are obtained with no prior hysteresis tests done to them, as it was detected that permanent deformation of the fabric was happening in these cases.

Two hypotheses are made in order to properly fit the data. It is assumed that the first specimen at the $[0/90]_2$ configuration is equivalent to a sample at the 1-direction. This may be seen as acceptable, as most of the load will be held up by the fabric at the 0° angle. The second assumption presumes that the sample in the $[45/135]_2$ configuration is equivalent to a simple shearing test. The reliability of this hypothesis may not be as sufficient as the first one, but since the stress levels are low for this test, in comparison to the first one, it is deemed adequate.

2.3. CAD and finite element model

Three modelling techniques were developed regarding the CAD drawings, as seen in Fig. 3. The first one assumes that the entirety of the rubber center has fiber-reinforced rubber properties. The second presumes that half the center contains fiber-reinforced rubber properties and the other half, only the elastomer properties. The third one has the assumption that two sets of reinforcements represented by surfaces S1 and S2 have the fabric material properties, while the rest of it have the pure elastomer material characteristics.

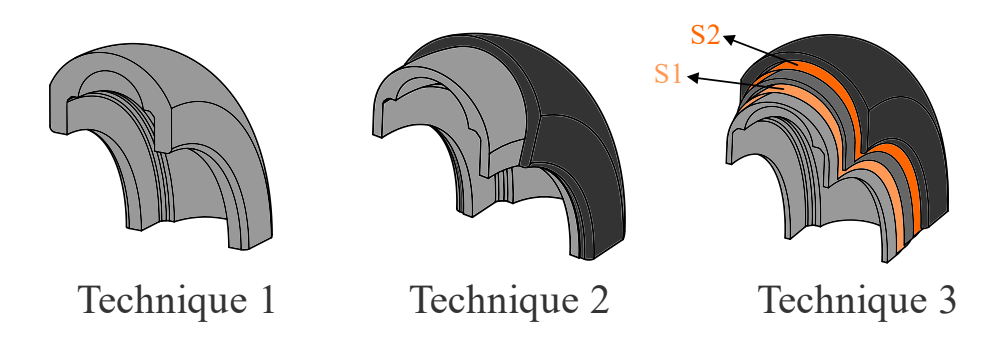


Figure 3 – Visualization for different CAD modelling techniques

Abaqus® software is employed in the finite element analysis. A prescribed displacement is implemented on both hubs, in order to force them against the rubber part, to simulate the bolt clamping force. Then, a torque of 500 Nm is applied to the model, while being clamped on one of the hubs' end surfaces. Tie restrictions are also applied between each part to restrain rigid body motion, while the bolts are modelled using Kinematic Couplings and Multi-Point Constraints (MPC). Figure 4(a) shows the clamped boundary condition and Fig. 4(b) presents the loads and the rest of the boundary conditions.

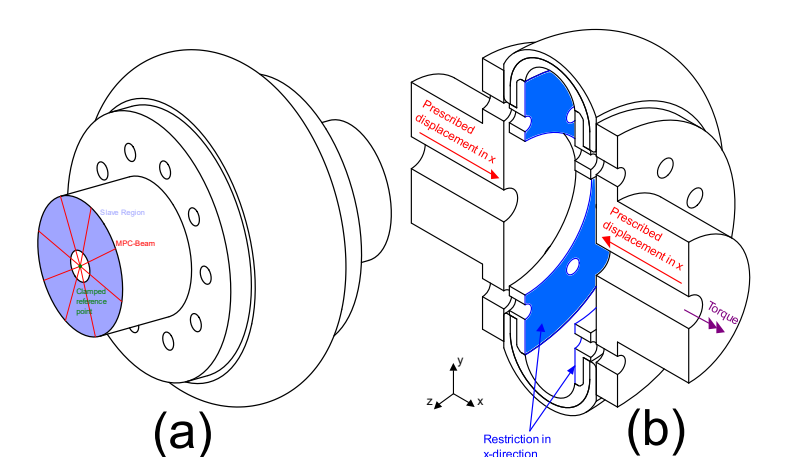


Figure 4 – (a) Clamped conditions for the model; (b) Prescribed displacements and torque.

A simple mesh study is carried out to access the quality of the results. Figure 5 shows how the stress values taken from a critical area of the coupling vary with different mesh refinements. A medium-sized mesh is utilized, which is not as computationally intensive as the fine mesh but is also able to properly present the results.

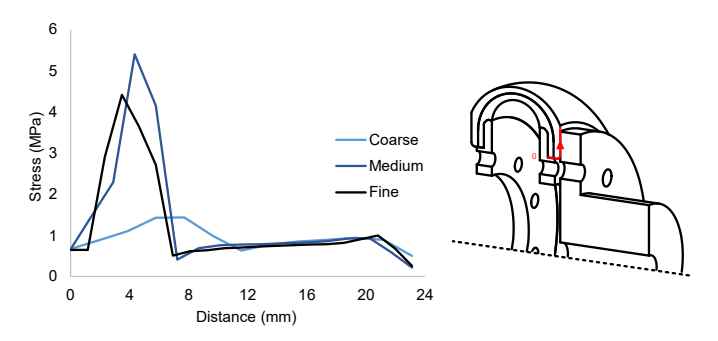


Figure 5 – Mesh study taken in a critical area.

3. RESULTS

Figure 6 shows the comparison between each employed technique along with the experimental results, which are made in a tire coupling subjected to a torque done by a universal testing machine through a special device. It is seen that Technique 2 can more precisely replicate the experimental behavior, although care should be taken, as the error becomes substantially greater the more torque is applied to the model. Nevertheless, there is good agreement with the experimental data up until values of approximately 300-400 Nm.

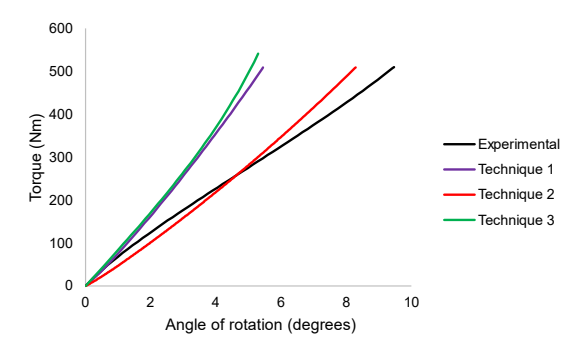


Figure 6 – Torque vs angle graph for experimental results and the three numerical techniques employed.

When looking at the values for stress, particularly from Fig. 7, one can see that the internal center area bears the highest values of stress. From a qualitative perspective, this is coherent, because the internal area is the one with the reinforced rubber properties, in which the calibration data included higher values of stress, when compared to only the pure elastomer experimental data. Also, the torque applied is expected to impose higher strains in the center of the toroidal structure.

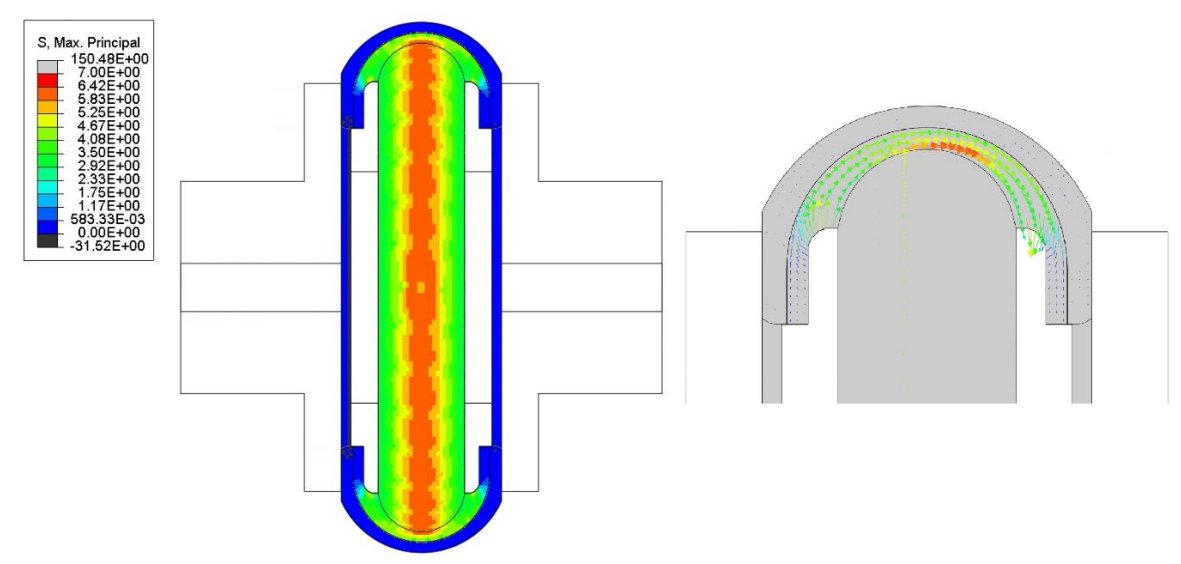


Figure 7 – Maximum principal stresses in the rubber center

In addition to it, from Fig. 8, the behavior observed in high torque values (in this case, 900 Nm or more) is also partially replicated in the numerical environment. The formation of what seems to be a local buckling from Fig. 8(c) is seen on both the stress and displacement simulation results.

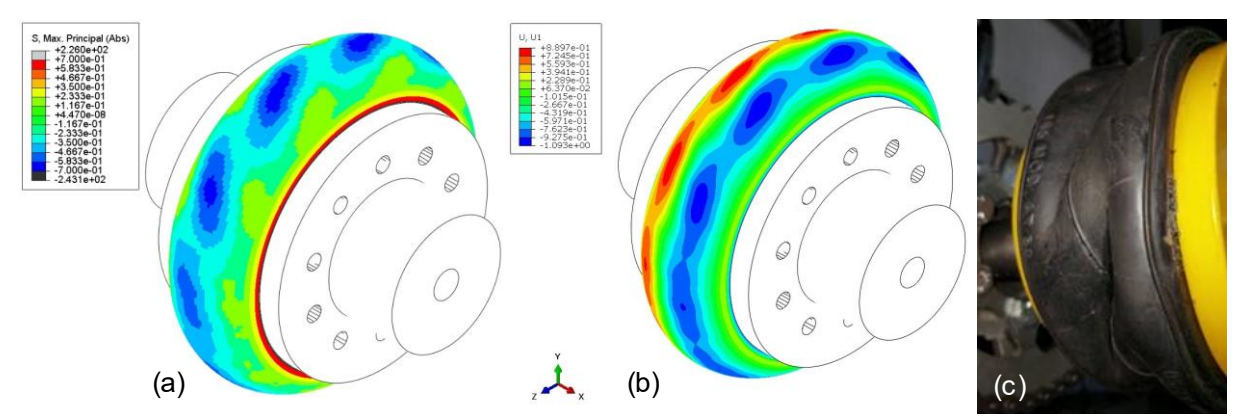


Figure 8 - (a) Maximum principal stress for high torque simulation, (b) Displacements in x-direction for high torque simulation and (c) Local buckling in flexible coupling obtained through application of high torque values.

4. CONCLUSIONS

In this work, several assumptions were made to evaluate the structural behavior of a fiber-reinforced rubber utilized in a tire coupling assembly. It was detected that, even though many simplifications had to be made in order to reach the results, the second modelling technique was able to depict the experimental behavior well within the same order of magnitude.

Finally, one can replicate the methodology used here to have an initial structural assessment of a fiber-reinforced elastomer component, as to how it might behave regarding its displacements and possible critical areas which may bear high stress sections.



ACKNOWLEDGEMENTS

This study was financed in part by the Coordenação de Aperfeiçoamento de Pessoal de Nível Superior - Brasil (CAPES). The authors would also like to thank Antares Acoplamentos LTDA for providing the materials and financial support that made this research possible.

REFERENCES

- [1] R. D. Vocke III, C. S. Kothera, B. K. S. Woods, et. al. Development and Testing of a Span-Extending Morphing Wing. Journal of Intelligent Material Systems and Structures, v. 22, p. 879-890. (2011).
- [2] M. Abbasi, M. S. Barakat, K. Vahidkhah, et. al. Characterization of three-dimensional anisotropic heart valve tissue mechanical properties using inverse finite element analysis. Journal of the Mechanical Behavior of Biomedical Materials, v. 62, p. 33-44. (2016).
- [3] P. Ciarletta, P. Dario, F. Tendick, et. al. Hyperelastic Model of Anisotropic Fiber Reinforcements within Intestinal Walls for Applications in Medical Robotics. The International Journal of Robotics Research, v. 28, p. 1279-1288. (2009).
- [4] G. Meschke, P. Helnwein. Large-strain 3D-analysis of fibre-reinforced composites using rebar elements: hyperelastic formulations for cords. Computational Mechanics, v. 13, p. 241–254. (1994).
- [5] L. W. Brown, L. M. Smith. A Simple Transversely Isotropic Hyperelastic Constitutive Model Suitable for Finite Element Analysis of Fiber Reinforced Elastomers. ASME. J. Eng. Mater. Technol, v. 133(2), 021021. (2011).
- [6] X. Peng, Z. Guo, T. Du, et al. A simple anisotropic hyperelastic constitutive model for textile fabrics with application to forming simulation. Composites Part B: Engineering, v. 52, p. 275-281. (2013).
- [7] Y. Wang, H. Zhou, Z. Liu, et al. A 3D anisotropic visco-hyperelastic constitutive model for unidirectional continuous fiber reinforced shape memory composites. Polymer Testing, v. 114, 107712. (2022).
- [8] X. Peng, G. Guo, N. Zhao. An anisotropic hyperelastic constitutive model with shear interaction for cord-rubber composites. Composites Science and Technology, v. 78, p. 69-74. (2013).
- [9] S. Ishikawa, A. Tokuda, H. Kotera. Numerical simulation for fibre reinforced rubber. Journal of Computational Science and Technology v. 2(4), p. 587-596. (2008).
- [10] G. A. Holzapfel, T. C. Gasser, R. W. Ogden. A new constitutive framework for arterial wall mechanics and a comparative study of material models. Journal of elasticity and the physical science of solids, v. 61, p. 1-48. (2000).



A 3D COMPUTATIONAL HOMOGENIZATION APPROACH FOR PREDICTING THE EFFECTIVE ELASTIC CONSTITUTIVE TENSOR OF PERIODIC POROUS MATERIALS

Wanderson Ferreira dos Santos^a, Sergio Persival Baroncini Proença^a

^aDepartment of Structural Engineering, Sao Carlos School of Engineering, University of Sao Paulo Av. Trabalhador Sao-Carlense, 400, ZIP 13566-590, Sao Carlos, SP, Brazil e-mail: wanderson_santos@usp.br, persival@sc.usp.br

Keywords: computational homogenization approach, periodic porous materials, effective elastic constitutive tensor, extrapolation strategy based on posteriori error estimation, results with accuracy

1. INTRODUCTION

Porous materials have been used in a wide range of industrial and engineering applications due to their interesting physical and mechanical properties. In this sense, porous solids are suitable materials in structures designed for lightweight materials, impact energy absorption, vibration and acoustic energy damping, for instance. Cellular and lattice materials are examples of porous structures with particular characteristics, including low density and large surface area. However, the effective constitutive behavior of porous solids can be complex due to the heterogeneity created by the voids. Therefore, the design of porous media requires detailed studies to obtain the desired properties.

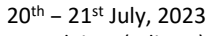
The study of the effective elastic properties of periodic structures can be important for the design of porous media. In particular, approaches based on computational homogenization are interesting to predict the effective elastic properties of porous materials [1]. In this context, the present work presents a computational homogenization framework for investigating the effective elastic constitutive tensor of periodic porous materials. In order to improve the accuracy of the computational approach, a strategy based on posteriori error estimation proposed by Szabó and Babuška [2] is explored to extrapolate the results from numerical simulations to estimate the components of the effective elastic constitutive tensor. The homogenization procedure is implemented in ANSYS® Mechanical-Release 18.0 using the Ansys Parametric Design Language (APDL). The consistency and applicability of the computational strategy is evaluated through the investigation of periodic porous materials. The numerical analyses are performed for RVEs composed of: (i) cubic cells with unidirectional voids of circular cross-section; (ii) cubic cells with unidirectional voids of square cross-section. The assessment of the void morphology can be of particular interest in the design of porous materials to obtain improved constitutive properties.

2. COMPUTATIONAL HOMOGENIZATION APPROACH

This section describes the 3D computational homogenization approach for predicting the effective elastic constitutive tensor of periodic porous media. The framework is implemented using the APDL language in ANSYS® Mechanical-Release 18.0. Constraint equations are explored to impose the periodic boundary condition given by

$$u = E^* \cdot x + \tilde{u} \quad \forall \quad x \in \partial V \tag{1}$$

where u is the displacement vector, E^* is the macroscopic strain tensor imposed on the RVE contour (∂V), \tilde{u} is the portion called periodic fluctuation, and x indicates the positions.





The solution of the Boundary Value Problem is obtained by solving the linear system of equations of the RVE through 3D numerical analyses performed with the Finite Element Method. The homogenized or macroscopic fields of stress (Σ) and strain (E) are calculated by:

$$\Sigma = \frac{1}{V} \sum_{i=1}^{\text{nelem}} \sigma_i V_i \tag{2}$$

$$E = E^{*}$$
 (3)

where *nelem* is the number of finite elements; σ_i is the average stress on the element i calculated from the values at its integration points; V_i is the volume of the element i; V is the total initial volume of the RVE (considering the hypothesis of small displacements). The macroscopic stress and strain tensors are linearly correlated by the effective constitutive tensor (\underline{C}):

$$\Sigma = \underline{\underline{C}} : E \tag{4}$$

The macroscopic constitutive behavior is assumed to be linear elastic obeying an orthotropic law. Different loading programs must be conveniently imposed on the RVE considering the homogeneous macroscopic strain tensor (E^*) to determinate the components C_{iikl} . Due to the symmetry of the problem: $C_{2222} = C_{1111}$; $C_{2233} = C_{1133}$; $C_{2323} = C_{1313}$. Therefore, the number of independent elastic components can be reduced to 6. In this context, each RVE is subject to 6 loading conditions: (1) $E_{11}^* = 1.0$; (2) $E_{22}^* = 1.0$; (3) $E_{33}^* = 1.0$; (4) $2E_{12}^* = 1.0$; (5) $2E_{23}^* = 1.0$; and (6) $2E_{13}^* = 1.0$.

The strategy proposed by Szabó and Babuška [2] is explored to estimate the effective elastic properties from the numerical results in order to improve the predictive ability of the computational approach. This strategy was initially proposed for a posteriori estimation of error in energy norm. However, the initial idea can be extended for predicting the effective properties. In this context, an effective elastic component (C_{iikl}) can be obtained from three numerical simulations (p, p-1 and p-2) solving the following non-linear equation:

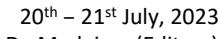
$$\frac{C_{ijkl} - C_{ijkl}^{(p)}}{C_{ijkl} - C_{ijkl}^{(p-1)}} \approx \left(\frac{C_{ijkl} - C_{ijkl}^{(p-1)}}{C_{ijkl} - C_{ijkl}^{(p-2)}}\right)^{Q}$$
(5)

where

$$Q = \frac{\log\left(\frac{N^{(p-1)}}{N^{(p)}}\right)}{\log\left(\frac{N^{(p-2)}}{N^{(p-1)}}\right)}$$
(6)

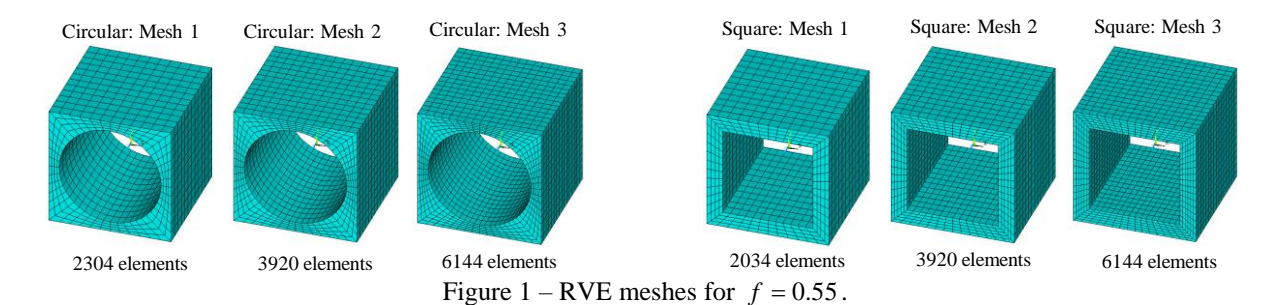
where N is the total number of degrees of freedom (D.F.) of each numerical simulation.

To illustrate the applicability of the computational framework, the influence of the void morphology on the effective elastic constitutive tensor of porous materials is assessed for cubes with unidirectional voids considering circular cross-section and square cross-section. Comparisons are performed for five porosity values: (i) f = 0.15; (ii) f = 0.25; (iii) f = 0.35; (iv) f = 0.45; (v) f = 0.55. Therefore, the analyses comprise a wide range of porosities. The microscopic constitutive behavior of the matrix is linear elastic, and the values for the modulus of elasticity (Y) and the Poisson coefficient (ν) are adopted according to Christoff et al. [1]: $Y_m = 70$ GPa and $\nu_m = 0.3$. Three numerical





simulations must be performed for each RVE to estimate a component of the effective elastic constitutive tensor by Eq. (1). For instance, Fig. 1 shows the simulated meshes in this paper for f = 0.55. The 20-node hexahedral finite element (H20) was used in numerical simulations.



3. RESULTS AND DISCUSSION

Initially, a comparative analysis was performed to assess the accuracy of the results extrapolated by Eq. (5) when compared to the analytical solution proposed by Rodríguez-Ramos et al. [3] and the numerical results in ABAQUS® software obtained by Christoff et al. [1]. Table 1 presents the comparisons performed for the RVE with a circular cross-section void and f = 0.55. The effective results obtained by the computational homogenization approach are close to the compared works. The proximity of the homogenized results with the analytical solution proposed by Rodríguez-Ramos et al. [3] indicates the consistency of the computational strategy herein proposed.

Table 1 – Results of the effective elastic stiffness tensor components compared with Rodríguez-Ramos et al. [3] and Christoff et al. [1] for the RVE with a circular cross-section void and f = 0.55.

		,				
	Rodríguez-Ramos et al. [3]	Christoff et al. [1]	Authors	Relative differences in mode		
Component	(1)	(2)	(3)	(2) to (1)	(3) to (1)	
C ₁₁₁₁ (GPa)	20.4986	20.5519	20.5015	0.2602%	0.0141%	
C_{3333} (GPa)	35.7979	35.8392	35.7986	0.1155%	0.0020%	
C_{1122} (GPa)	3.3787	3.3881	3.3783	0.2782%	0.0127%	
C_{1133} (GPa)	7.1632	7.1820	7.1650	0.2627%	0.0251%	
C_{1212} (GPa)	1.8088	1.8276	1.8101	1.0431%	0.0708%	
C_{1313} (GPa)	7.4591	7.4795	7.4605	0.2739%	0.0182%	

The extrapolated results for the components of the effective stiffness tensor considering different RVE morphologies are shown in Fig. 2. The results are presented for porosities between f = 0.15 and f = 0.55, in which 180 numerical simulations were computed for predicting the effective properties. For lower porosity values, in general, the RVE with a unidirectional void of circular crosssection provides more stiffness when compared to the RVE with a unidirectional void of square crosssection. The biggest relative differences occur for the component C_{1212} , which is directly associated with the shear modulus in plane of the void cross-section. It is also worth mentioning the differences in the case of component C_{1122} . In relation to component C_{1212} , the differences are more evident with the increase in porosity. Furthermore, the differences are also sensitive for the component C_{1133} considering lower porosity values. On the other hand, except for C_{1122} and C_{1212} , the component results are closer for high porosity values. Therefore, the void morphology and the porosity level can strongly influence the effective constitutive tensor of the porous material with periodic behavior.

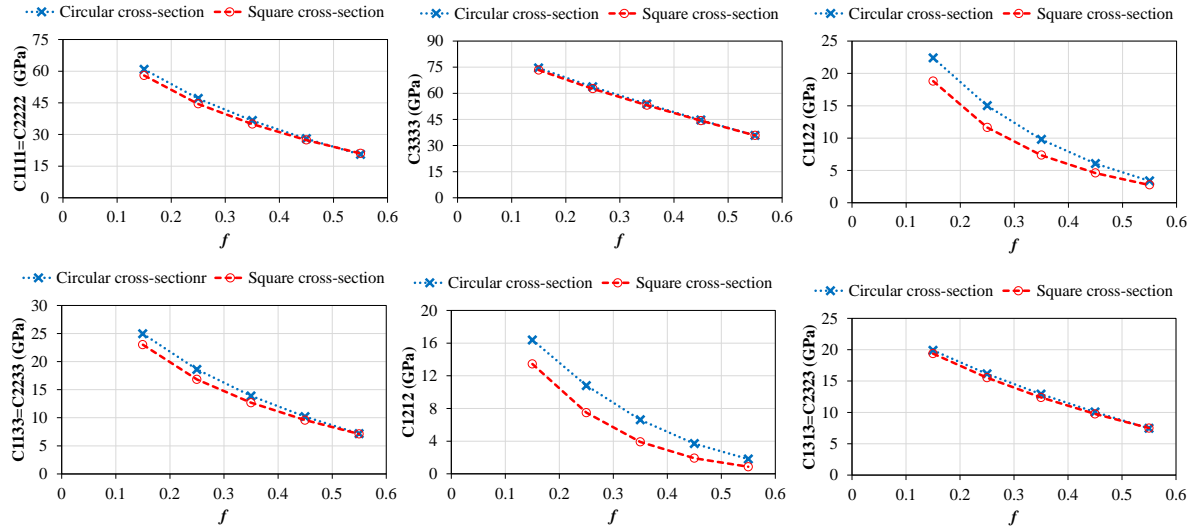


Figure 2 – Effective elastic stiffness components for the RVEs with different void morphologies and porosities.

4. CONCLUSIONS

In this paper, a computational homogenization approach was proposed for predicting with good accuracy the effective elastic constitutive tensor of periodic porous materials. In particular, an extrapolation strategy was explored to better estimate the final homogenized results from the numerical results computed by a computational homogenization procedure implemented using the APDL language in ANSYS® Mechanical, Release 18.0. The applicability of the computational strategy was investigated by a study considering the influence of the void morphology on the effective elastic constitutive tensor of porous materials with periodic structure. The study was performed for unidirectional voids of circular and square cross-sections with different porosity values.

The accuracy of the approach based on computational homogenization was assessed by means of comparisons with other works in the literature, including analytical and numerical studies. In this context, the final results showed good agreement with the compared works for unidirectional voids of circular cross-section, evidencing the consistency of the computational strategy. In particular, the effective results were very close to the results of the compared analytical approach, where the differences were minimal. The comparison between the different void morphologies showed interesting conclusions. In general, significant differences were observed for the components of the effective elastic constitutive tensor associated with the shear in the plane that cuts the void crosssection. Finally, it is worth mentioning that the computational homogenization framework herein described is an interesting strategy for the design of periodic porous materials with improved and/or specific effective properties, including applications in cellular and lattice structures.

REFERENCES

- [1] B.G. Christoff, H. Brito-Santana, R. Talreja, et al. Development of an ABAQUS plug-in to evaluate the fourth-order elasticity tensor of a periodic material via homogenization by the asymptotic expansion method. Finite Elements in Analysis and Design, v.181, p. 1-13. (2020).
- [2] B. Szabó, I. Babuška. *Finite element analysis*. Wiley-Interscience. New York. 1st ed. (1991).
- [3] R. Rodríguez-Ramos, R. Medeiros, R. Guinovart-Díaz, et al. Different approaches for calculating the effective elastic properties in composite materials under imperfect contact adherence. Composite Structures, v.99, p. 264-275. (2013).

RESPONSIBILITY NOTICE

The authors are the only responsible for the printed material included in this manuscript.



ON THE USE OF A NOVEL ALL-SOLID-STATE BATTERY AS A COMPOSITE STRUCTURE DAMAGE SENSOR

Denys Eduardo Teixeira Marques^a, Bruno Guilherme Christoff^b, Maísa Milanez Maciel^a, Pouria Ataabadi^c, João Paulo Carmo^d, Maria Helena Braga^e, Rui Guedes^b, Marcílio Alves^c, Volnei Tita^{a,b}

^a University of São Paulo, São Carlos School of Engineering Aeronautical Engineering Department, Av. João Dagnone 1100, São Carlos, SP, Brazil denysmarques@gmail.com, voltita@sc.usp.br, maisa.madm@usp.br

^bUniversity of Porto, Faculty of Engineering of the University of Porto Mechanical Engineering Department, Rua Dr. Roberto Frias s/n, Porto, Portugal bchristoff@fe.up.pt, rmguedes@fe.up.pt

^cUniversity of São Paulo, Engineering School of the University of São Paulo Mechanical Engineering Department, Av. Prof. Mello Moraes 2231, São Paulo, SP, Brazil pouriabahrami@usp.br, maralves@usp.br

^dUniversity of São Paulo, São Carlos School of Engineering Electrical Engineering Department, Av. Trabalhador São Carlense 400, São Carlos, SP, Brazil jcarmo@sc.usp.br

^eUniversity of Porto, Faculty of Engineering of the University of Porto Department of Engineering Physics, Rua Dr. Roberto Frias s/n, Porto, Portugal mbraga@fe.up.pt

Keywords: All-Solid-State Battery, Piezoelectricity, Vibrational Test

1. INTRODUCTION

In the last decades, the use of battery technologies, especially lithium-ion (Li-ion), has been a very important trend for numerous electrical applications. The combination of high energy and power density makes it a substantial solution in applications such as portable electronic devices and vehicles. This type of battery has, however, a couple of limitations, such as slow charging, and a flammable electrolyte [1].

Aiming at greener energy storage, and more efficient and safer types of batteries, companies and governments have invested great amounts of money in developing newer technologies for energy storage [2]. Thus, the development, production, and use of environmentally friendly batteries are the key to achieving a sustainable, and climate-neutral technology [3].

An alternative to the well-established Li-ion battery is the use of solid-state electrolytes, which have been attracting significant attention due to their advantages, such as non-flammability, higher thermal stability, no leakage risk, and non-volatile materials. In addition, this alternative also demonstrates better mechanical properties and a higher electromechanical window of stabilities in comparison to the Li-ion counterpart, making it an interesting alternative in energy technology [4].

Considering the aforementioned aspects, the present study considers a novel all-solid-state battery to investigate the possibility of using it as a piezoelectric sensor. Figure 1(a) shows a depiction of the battery used, in which the electrodes are made of Zinc and Copper, and the electrolyte is formed by a Sodium solution. The battery is coated with a polymeric protective film, as shown in Figure 1(b).

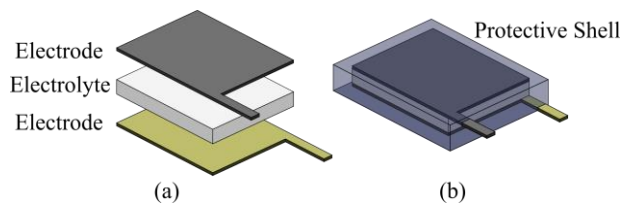


Figure 1 – Schematics of the all-solid-state battery: (a) electrodes and electrolyte; (b) battery assemble and protective polymeric shell.

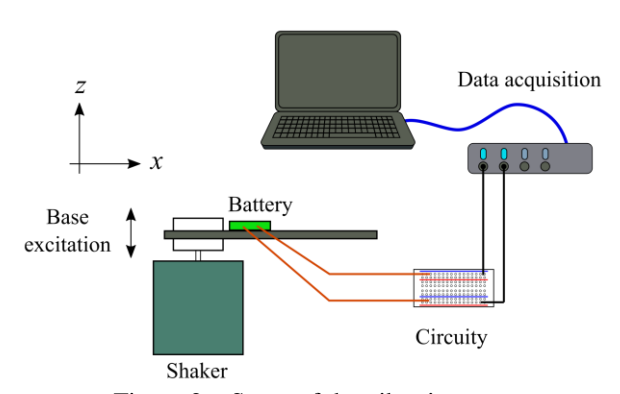
In this work, the objective is to use an all-solid-state battery as a piezoelectric sensor and to discuss the potentialities and limitations of this type of battery for such applications. Thus, vibrational tests are performed using this battery coupled to a composite beam and a shaker. The battery signal variation is obtained when the battery is subjected to constant vibration. This type of test seeks to understand the potential of applying this type of battery as a sensor, which can be very promising in several engineering applications.

2. EXPERIMENTAL SETUP

To evaluate the piezoelectric response of the battery, a case study is examined using a composite carbon fiber beam. The geometry is that of a cantilever beam with 2.2 mm thickness, 30 mm width, and 150 mm long. The battery is attached to the beam and it is positioned close to the clamp device, as schematically shown in Figure 2.

The beam is clamped to a rigid grip, which is then mounted on an electrodynamic shaker, subjecting the specimen to a base excitation condition. The shaker is set to produce a constant frequency sine wave signal, and the response of the battery at different excitation frequencies is examined. It should be noted that the first bending mode of the beam is located at around 90 Hz, while the second bending mode is found only at 350 Hz. The base-acceleration load is applied in the z-direction (as shown in Figure 2), and in some tests, an added mass is glued to the free tip of the beam, thus increasing its vibration amplitude.

The battery is connected to a circuity mounted directly into a breadboard, which is designed to remove its DC output voltage but allowing the passage of the voltage oscillations expected to happen during the vibration tests. The signal is then sent to a Kistler LabAmp 5167A data acquisition system.



 $Figure\ 2-Setup\ of\ the\ vibration\ test.$

The battery is attached to the beam using a rapid curing, single component adhesive, and it is positioned close to the clamp device, as schematically shown in Figure 3. In addition, two accelerometers are used for comparison measures. The first accelerometer is attached to the rigid grip to measure the base acceleration. The second accelerometer is attached to the tip of the beam, and its signal is compared to the battery signal.

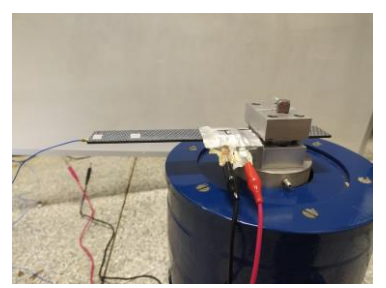


Figure 3 – Depiction of the battery attached to the composite beam mounted to the shaker.

3. RESULTS AND DISCUSSION

In a preliminary study, the battery behavior under a constant base excitation of the system is investigated. An excitation frequency of 25.0Hz is chosen for the vibrational tests since this frequency is sufficiently distant from the natural frequencies of the system. The vibrational test is initiated with the shaker off, and then it is suddenly turned on, and after a few seconds, it is turned off again. The time signal of the battery and the highlights of the regions in which the shaker is off and on are shown in Figure 4.

In the region where the shaker is turned on, it is noticed that the battery is capable of generating a variation in the electrical potential difference at the same excitation frequency as the system, that is, 25.0Hz. Another characteristic noted in the test is that in regions where the shaker is turned off, the battery signal oscillates at a frequency of 60.0Hz, due to electromagnetic interference from the electrical network.

It is important to note that the amplitude of the battery signal when the shaker is on is about 10 times greater than the amplitude of the signal when the shaker is off. In this way, the battery can generate a representative electrical signal for the analyzed case, even with the noise coming from the electrical network.

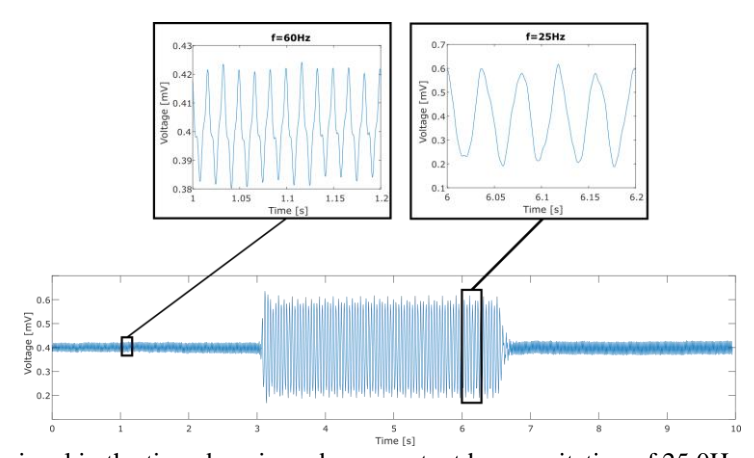
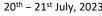


Figure 4 – Battery signal in the time domain under a constant base excitation of 25.0 Hz - shaker is suddenly turned on and then turned off after a few seconds, and highlights of the regions where the shaker is off and on.

In a following analysis, the battery signal in the frequency domain is investigated. Thus, the Fast Fourier Transform (FFT) is used to convert the signal in the time domain to the frequency domain. Figure 5 shows the battery signal in the frequency domain, as well as the signal of the accelerometer on the tip of the beam. It can be seen that both the battery and the accelerometer can detect signal peaks at the working frequency of the system (25.0Hz), as well as its harmonics (multiples of 25.0Hz). In addition, it can be seen that the battery presents signal peaks in frequencies multiple of 60.0Hz, due to electromagnetic interference due to the electrical network.

As initial conclusions, it can be said that there are possibilities of using the battery as a piezoelectric sensor since it generates a potential difference when excited at a constant frequency. Also,





the amplitude of the signal generated by the battery when excited is much higher than the amplitude of the signal due to electromagnetic noise.

For future work, the battery will be excited at different frequencies to investigate the limit of battery usage. The higher the excitation frequency of the system, the smaller the signal amplitude generated by the battery. Thus, we have to investigate at what working frequency level the signal amplitude generated by the battery is equal to or less than the electrical network noise, which implies the impossibility of using the battery at these frequencies.

Hereafter, we will use a sweep-type excitation signal, to find the natural frequencies of the system through the signal generated by the battery. Finally, aiming at applications in Structural Health Monitoring (SHM), the battery will be used to compare systems using an intact beam and a damaged beam. With this investigation, it will be possible to determine if the signal generated by the battery is capable of detecting variations in the natural frequencies of the system, due to damage to the composite beam.

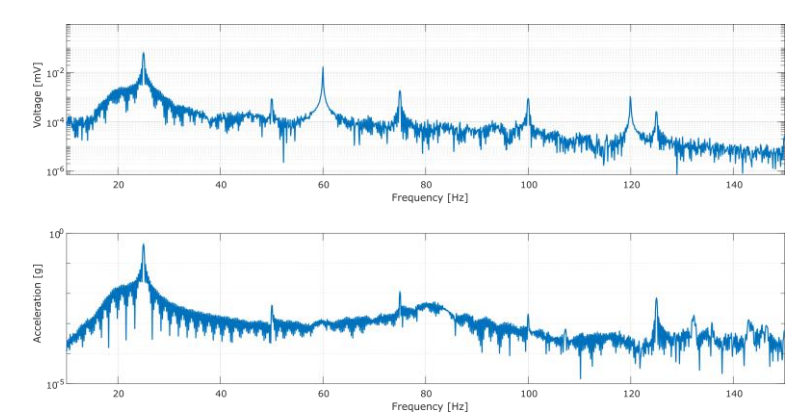


Figure 5 – Battery and accelerometer signals in the frequency domain.

ACKNOWLEDGEMENTS

Volnei Tita acknowledges the financial support of the National Council for Scientific and Technological Development (CNPq process number: 310656/2018-4). The authors are thankful for the support of the Coordenação de Aperfeiçoamento de Pessoal de Nível Superior – Brasil / Finance Code 001, and for the support of Dean's Office of Researcher of the University of São Paulo via "PIPAE -PROJETOS INTEGRADOS PARA PESQUISAS EM ÁREAS ESTRATÉGICAS".

REFERENCES

- [1] F. Danzi, P.P. Camanho, and M.H. Braga. An all-solid-state coaxial structural battery using sodium-based electrolyte. *Molecules*, v.26(17), p.5226. (2021).
- [2] F. Danzi, R.M. Salgado, J.E. Oliveira, et al. Structural batteries: A review. *Molecules*, v.26(8), p.2203. (2021).
- [3] F. Danzi, M. Valente, S. Terlicka, et al. Sodium and potassium ion rich ferroelectric solid electrolytes for traditional and electrode-less structural batteries. APL Materials, v.10(3), p.031111. (2022).
- [4] M.C. Baptista, H. Khalifa, A. Araújo, et al. Giant Polarization in Quasi-Adiabatic Ferroelectric Na+ Electrolyte for Solid-State Energy Harvesting and Storage. Advanced Functional Materials, p.2212344. (2022).

RESPONSIBILITY NOTICE

The author(s) is (are) the only responsible for the printed material included in this manuscript.



VERTICAL TWO-PHASE FLOW WITH A NON-NEWTONIAN PHASE IN LAMINAR HETEROGENEOUS POROUS MEDIA

Lucas Constantino Mendonça^a, Panters Rodríguez-Bermudez^a, Alexandre Santos Francisco^a, Isamara Landim Nunes Araujo^b, Jorge A. Rodríguez Durán^c

^aPPG-MCCT, Universidade Federal Fluminense (UFF) Av. dos Trabalhadores 420 Vila Sta. Cecília, Volta Redonda -RJ 27255-125, Brasil lucasconstantino@id.uff.br pantersrb@id.uff.br afrancisco@id.uff.br

bIMECC/UNICAMP

Rua Sérgio Buarque de Holanda 651, Campinas-SP 13083-859, Brasil Isamara-landim@hotmail.com

^cUniversidade Federal Fluminense (UFF) Av. dos Trabalhadores 420 Vila Sta. Cecília, Volta Redonda -RJ 27255-125, Brasil jorgeduran@id.uff.br

Keywords: flow in porous media, heterogeneous porous media, two-phase flow, non-Newtonian fluids, gravity

1. INTRODUCTION

In the oil and gas industry, natural production mechanisms allow for the recovery of an average of 20 to 40% of the total oil contained in the reservoir. In view of this, secondary and enhanced recovery methods are used aiming at a greater oil recovery or maintenance of reservoir pressure [1]. The most used methods in secondary recovery are waterflooding (immiscible water injection) and immiscible gas injection. During the application of the immiscible water injection method, if the displaced fluid is a very viscous oil, it may possess rheological attributes characteristic of that of a non-Newtonian fluid, while in enhanced oil recovery, some methods utilize surfactant, alkaline, or polymer solutions, which can impart non-Newtonian behavior to the injected fluid [4]. The great frequency in the use of such methods becomes a motivation for carrying out several studies aimed at simulating the flow of Newtonian and non-Newtonian fluids in porous media. A variety of physical phenomena such as the two-phase immiscible flow of fluids in porous media, for example, can be modeled through conservation laws and the well-known Riemann problems (piecewise constant initial data). For heterogeneous porous media, obtaining Riemann solutions analytically can be a very tough task, so numerical methods have been increasingly used to obtain approximate solutions to a given problem. In problems involving conservation laws with piecewise constant data, the methods of Godunov, Lax-Wendroff, MacCormack and Lax Friedrichs are highlighted [5].

2. MATHEMATICAL MODEL

The present research proposes the study of a mathematical model for vertical two-phase immiscible flow in heterogeneous porous media with a non-Newtonian phase of Bingham plastic type based on an extension of the Buckley-Leverett equation [6]. The heterogeneous rock is assumed to be a composite porous material composed by a periodic-laminar structure with two types of rocks, one of





them as a matrix while the other is a refill. In parallel, the finite difference numerical schemes of Lax-Friedrichs and Lagrangian-Eulerian developed by [2] were implemented.

2.1. Darcy's law and apparent viscosity for Bingham plastic

In order to carry out a phenomenological description of the flow of non-Newtonian fluids, such as Bingham plastic, through porous media, it is necessary to take into account the apparent viscosity of the rheological model in question within Darcy's Law. A modified version of Darcy's Law for non-Newtonian fluids of the Bingham plastic type is presented as follows:

$$u = \begin{cases} \frac{-K}{\mu_B} \left(1 - \frac{G}{|\nabla \Phi|} \right) |\nabla \Phi|, if |\nabla \Phi| > G, \\ 0, if |\nabla \Phi| \le G, \end{cases} \tag{1}$$

where

$$|\nabla \Phi| = |\nabla P| \pm \rho g. \tag{2}$$

The apparent viscosity can be obtained by rearranging Eq. (1) and after some algebraic manipulations, the following expression is achieved:

$$M(\nabla \Phi^*, S_{Ne}) = \frac{\mu_{Ne}}{\mu_{nN}} = \begin{cases} \frac{1}{m_{\alpha}} \left(1 - \frac{G^*}{|\nabla \Phi^*|} \right) |\nabla \Phi^*|, & \text{if } |\nabla \Phi^*| > G^*, \\ 0, & \text{if } |\nabla \Phi^*| \le G^*, \end{cases}$$

$$\tag{3}$$

where u is the Darcy velocity vector, μ_B is the consistency index of the rheological model, G is the minimum pressure gradient, $G^*=G/\gamma_{nN}$ is the dimensionless minimum pressure gradient, K is the absolute permeability of the rock, ∇P is the pressure gradient, $\nabla \Phi$ is the flow potential gradient, $\nabla \Phi^*$ is the dimensionless flow potential gradient (see [6]), ρ is the fluid density, μ_{Ne} is the dynamic viscosity of Newtonian phase, μ_{nN} is the apparent viscosity of non-Newtonian phase, $m_{\alpha} = \mu_B/\mu_{Ne}$ and g is the gravitational constant. Once the variables are defined, it is important to mention that if G^* equals zero, the problem goes back to the Newtonian case.

2.2. Two-phase flow with a non-Newtonian phase in heterogeneous porous media

For a laminar flow in a porous medium composed of two rocks with distinct absolute permeabilities, we should define:

$$\frac{\partial S}{\partial t} + \frac{\partial f_l(S)}{\partial Z}, if \ Z < 0; \frac{\partial S}{\partial t} + \frac{\partial f_r(S)}{\partial Z}, if \ Z > 0,$$

$$S(Z,0) = \begin{cases} S_l, if \ Z < 0, & \text{with } f_l(S_l) = f_r(S_r) \\ S_r, if \ Z > 0, & \text{with } f_l(S_l) = f_r(S_r) \end{cases} \tag{4}$$

Here f_l , f_r : [0,1] \rightarrow R are the flux functions assumed to be twice differentiable such that $f_l(0) =$ $f_r(0)$ and $f_r(1) = f_r(1)$, S is the fluid saturation and Z is the vertical coordinate. The flux function for the Newtonian phase, considering it as the displacing phase (the phase that displaces the non-Newtonian phase) for vertical flow (with gravity), can be represented in the following manner:

$$f_{Ne_L} = \frac{1}{1 + \frac{(1 - S_{Ne})^2}{S_{Ne}^2} M(\nabla \Phi^*, S_{Ne})} \left[1 + N_g (1 - S_{Ne})^2 \right], \tag{5}$$

and

$$f_{Ne_R} = \frac{1}{1 + \frac{(1 - S_{Ne})^2}{S_{Ne}^2} M(\nabla \Phi^*, S_{Ne})} \left[1 + K_f N_g (1 - S_{Ne})^2 \right], \tag{6}$$

with $K_f = K_{r/} K_l$, where K_r is the absolute permeability of the right rock layer, K_l is the absolute permeability of the left rock layer and $N_g(\nabla \Phi^*, S_{Ne})$ is a gravitational parameter [6].





RESULTS AND DISCUSSION

In the present research, two cases are presented. For the first case, $|\nabla \Phi^*|$ was considered greater than G^* , while for the second case, $|\nabla \Phi^*|$ was considered less than or equal to G^* . For Case I, the following dimensionless parameters associated with $\nabla \Phi^*$ were considered: node number = 5000, CFL = 0.6, T=1, $S_l=0.3$, $S_r=0.7$, number of time steps = 1027, $m_\alpha=4$, $\eta=2.5$, $G^*=0.375$, $\gamma*=1.25$, $\omega*=5$, and $K_f=0.5$. As for Case II, the following parameters were considered: node number = 5000, CFL = 0.6, T=2, $S_l=0.8165$, $S_r=0$, number of time steps = 246, $m_\alpha=0.1$, $\eta=0.025$, $G^*=0.625$, $\gamma*=1.25$, $\omega*=0.125$, $K_f=2$, $K_f=0.8165$ and $K_f=0.8165$

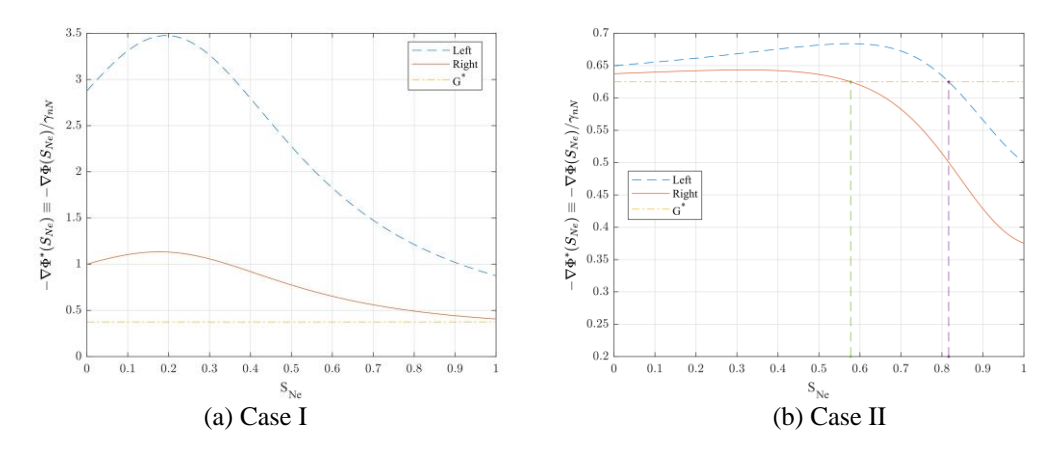


Figure 1 – Flow potential gradient.

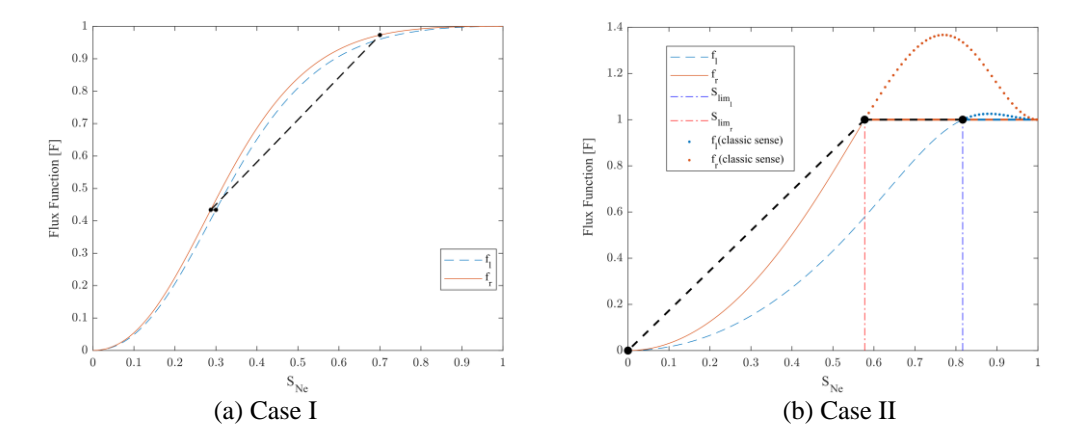


Figure 2 – Flux functions.



(a) Case I

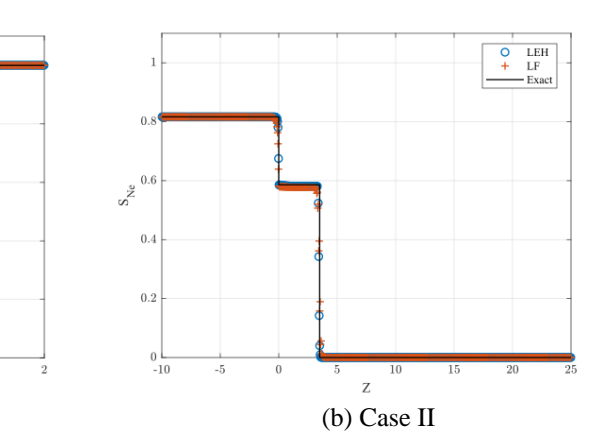


Figure 3 – Analytical and numerical solutions.

The numerical solutions obtained were compared with the analytical solutions determined through the extension of Oleinik's geometric construction to discontinuous flux functions emerged as a consequence of the heterogeneity in the rock. The numerical results were satisfactory when compared with the exact solutions that consist of the combination of shock waves, with the presence of a stationary shock at the point of discontinuity (interface between the two types of rocks) of spatial variable.

The solutions of both cases consist of a positive-speed shock wave and a stationary shock wave. What differentiates the solutions is the existence of a limiting saturation, which determines the maximum Newtonian-phase saturation value at which the fluid continues to behave as a liquid. This phenomenon is observed in Case II, which presents a limiting saturation of 0.8165 for the rock layer on the left side. This behavior is due to the rheological model, as for saturations above the limiting saturation, the apparent viscosity becomes infinite, and the fluid does not flow.

REFERENCES

- [1] A. Bahadori. Fundamentals of enhanced oil and gas recovery from conventional and unconventional reservoirs. Gulf Professional Publishing. 1nd edition. (2018).
- [2] E. Abreu and J. Pérez. *A new locally conservative lagrangian eulerian method for hyperbolic and balance laws*. In: VIII Pan-American Workshop Applied and Computational Mathematics. (2014).
- [3] L. C. Mendonça. *Mathematical and computational modeling of biphase flow in heterogeneous porous media under gravitational effect and the presence of non-Newtonian phase*. Master Thesis. Federal Fluminense University. (2023).
- [4] N. El-Khatib. Immiscible displacement of non-Newtonian fluids in communicating stratified reservoirs. *SPE Reservoir Evaluation & Engineering*, v.9, n. 04, p. 356-365, August. (2006).
- [5] R. J. LeVeque. Numerical Methods for Conservation Laws. Basel: Birkhäuser. (1992).
- [6] Y. S. Wu. *Multiphase fluid flow in porous and fractured reservoirs*. Gulf Professional Publishing. 1nd edition. (2015).

RESPONSIBILITY NOTICE

The author(s) is (are) the only responsible for the printed material included in this manuscript.